THE EFFECTS OF HEART RATE ON BLOOD FLOW IN INTRACRANIAL ANEURYSMS

by

HÅKON ØSTERBØ

THESIS

for the degree of

MASTER OF SCIENCE

(Master i Anvendt matematikk og mekanikk)

Faculty of Mathematics and Natural Sciences
University of Oslo

June 2013

Det matematisk- naturvitenskapelige fakultet
Universitetet i Oslo

Acknowledgements

First of all I want to thank my supervisors Kent-Andre Mardal, Øyvind Evju and Martin Sandve Alnæs. I appreciate all the help I have gotten from discussions to e-mail answers at 9 o'clock on a Sunday. I am grateful to Simula Research Laboratory for meshes, Doppler images and computational power that have made this thesis possible.

I would like to thank my mother Dagny, Jarle, Marius, Mikkel, Oda, my father Olav, Solfrid and my sister Sunniva for constructive feedback on my thesis. Also thanks my fellow students in B1002 for a great working environment and to all the friends I have met during these five years of study.

Last but not least thanks to Caroline for being a patient and supportive girlfriend these last months.

Notation

Ω	A subdomain in $\mathbb{R}^n$.
$\Omega(t)$	A subdomain in $\mathbb{R}^n$ that varies with time t.
$\partial\Omega$	The boundary of Ω.
$L^p(\Omega)$	Legesgue space p.
$C^p(\Omega)$	Space of functions which are p times differentiable.
$C_0^p(\Omega)$	Space of functions which are p times differentiable with compact support.
u	Velocity field. We will not use common bold notation for vector functions as it will become clear due to the context if a function is vector or not.
n	The outward pointing normal of the boundary of a given domain. In the case of an integral the domain will be the one that is integrated over.
$\mathrm{d}x$	We will use x as our variable over integration for all volume integrals, and it will be assumed that the functions to be integrated are functions of x.
$\mathrm{d}S$	We will use $\mathrm{d}S$ to denote surface integration.
$(u, v)_\Omega$	The inner product in L^2. Defined as $\int_\Omega uv \, \mathrm{d}x$ for scalars, $\int_\Omega u \cdot v \, \mathrm{d}x$ for vector functions and $\int_\Omega u : v \, \mathrm{d}x$ for matrices.
$\|u\|_{L^2(\Omega)}$	The norm of L^2. Defined as $\sqrt{(u, u)_\Omega}$.
$\|a\|$	The absolute value of a for a scalar or the Euclidean norm for vectors.
$\overline{S}$	Averaging operator over time.
W_k^p	Sobolev space.
H^1	The Sobolev space W_1^2.
CG_q	Continuous Galerkin space.

Contents

Chapter 1

Introduction

An aneurysm is an acquired abnormal dilation of a blood vessel caused by a weakness in the vessel wall. Aneurysms in the brain are called intracranial aneurysms. It is believed that the movement of the blood and the force it exerts on the wall of the blood vessel plays a key role in aneurysm formation and progression [5]. The hemodynamic forces splits into forces that act normal and parallel to the wall. The parallel force is often called wall shear stress (WSS), and is caused by the friction between the wall and the moving blood. In Chapter 2 we explain more about the severity of the aneurysm phenomena.

The blood flow in an aneurysm can be calculated using a 3-D description of the aneurysm and solving the famous Navier-Stokes equations. This require good 3-D imaging techniques and access to enough computational power both of which have been achieved these past two decades. These breakthroughs has encouraged a lot of research into using computational fluid dynamics (CFD) to investigate aneurysms. Measures for detecting aneurysm formation, growth or rupture have been studied [3, 12, 17, 22, 27] and the WSS is usually a key part in these measures. Whether high or low WSS is a cause of growth or rupture in aneurysms is not known and contradictory results have been made [20]. Other research have focused on assumptions and variables in the simulation model. The emphasis have mostly been on the effects of assuming rigid artery walls, modeling blood with constant viscosity (i.e. assuming blood is a Nwetonian fluid) and various outflow boundary conditions (these assumptions will be explained in Chapter 3). The implications of using different heart rates as inflow conditions however have not been studied extensively to our knowledge. One study [11] have examined heart rate changes in two aneurysms. They explored the nature of vortex formation and stress distribution in the aneurysm. The conclusion was that the flow became more complex and stress

on the aneurysm rose as the heart rate increased. They did not compare the changes to other common variables.

We will in this study investigate the difference in blood flow pattern and WSS between high and low heart rate in aneurysms. Proper orthogonal decomposition (POD), described in Chapter 5, will be used to quantify the complexity of the flow. We will investigate these changes in twelve different patient specific aneurysms. The results we find will be set in context with the changes in modeling blood with a varying viscosity.

Logically one might assume that an elevated heart rate will enhance the risk of rupturing an aneurysm, as the blood changes more rapidly and exerts higher levels of stress on the vessel (even though it has not been shown that high stress relates to rupture). However, the relationship between heart rate and rupture is hard to examine as one have to rely on interviewing patients about their activity before the time of rupture and in many cases it is impossible to gain that information due to disability or death. Even though the evidence is not sufficient to draw a definitive conclusion, some studies have shown a positive correlation between physical exercise and rupture of aneurysms [1, 19].

CFD may one day become a powerful tool used in medicine. Serving as a good way to decide whether or not to precede with medical treatment, and if so decide on the best available treatment. This is highly relevant for patients with aneurysms considering the high uncertainty of success that different treatments have. CFD analysis may be able to help assess the risk of rupture versus the risk of medical treatment. With computers it is possible to run simulations of different scenarios and find the consequences without risking complications to the patient.

The power of CFD is that time and space can be discretized to a very high accuracy. This makes quantities such as stress from the blood easier to obtain with higher sample rate and accuracy.

We will use a finite element library called FEniCS to implement the computational models in this thesis. Using highly optimized second hand tools it solves the matrix equations wrapped in a python interface called Dolfin. This makes it easy to solve complicated equations, which the Navier-Stokes equations are, in a highly efficient way. A modified verson of nsbench[1] will be used as our solver which is compatible with FEniCS version 1.2. Source code can be found at http://folk.uio.no/haakonoo/master/sourcecode/.

[1] Code can be found at https://launchpad.net/nsbench/.

Chapter 2

Medical background

An aneurysm is an acquired, abnormal dilation of a blood vessel that is caused by a weakness in the vessel wall. Aneurysms often look like balloons attached to the vessel. These are called saccular aneurysms. Different kinds of aneurysms exist, but these are uncommon and will not be discussed in this thesis. Saccular aneurysms are split into bifurcation aneurysms; where the aneurysm lies in the division between two branching blood vessels and sidewall aneurysms, where the aneurysm is placed on one side of the vessel wall. It is belived that an aneurysm will rupture when the wall tension exceeds the strength of the wall.

Intracranial aneurysms mostly occur in and around the Circle of Willis (CoW); a series of arteries coupled together at the base of the brain (see Figure 2.1). These vessels in the brain course through the subarachnoid space which is an area located between the skull and the brain. Filled with a liquid it protects the brain from damage. If an aneurysm rupture, blood will flow into the subarachnoid space causing subarachnoid haemorrhage (SAH).

The incidence of SAH due to a ruptured aneurysm is about 9 per 100000 people per year [6]. The consequences of a ruptured aneurysm may be fatal. The mortality and morbidity rates of ruptured aneurysms are 50% and 30% respectively [4, 26]. Considering that the general mortality rate is about 800 per 100000 per year [9][1], deaths due to ruptured aneurysms is a large portion of that rate and makes it well worth studying to gain a better understanding of the overall phenomena.

[1]The mortality rate varies from country to country. The number given is for the U.S. in 2010

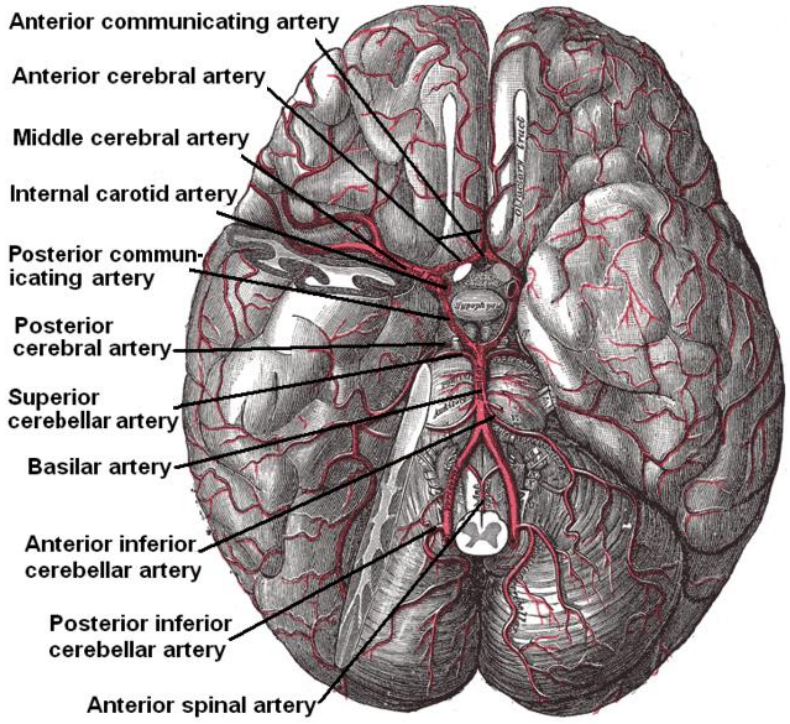

Figure 2.1: Illustration the blood vessels in the brain. The Circle of Willis consists of the following arteries: Anterior cerebral artery (ACA), Anterior communicating artery (ACOMA), Internal carotid artery (ICA), Posterior cerebral artery (PCA), Posterior communicating artery (PCOMA), basilar artery (BA) and Middle cerebral artery (MCA).

Since they rarely experience any form of symptoms patients with aneurysms are often not aware of their condition. Several studies have been conducted to find the occurrences of intracranial aneurysms in the general population, with results ranging from less than 1% to over 10%. Though most studies states the prevalence within the range of 5% to 7% [21].

The overall causes of aneurysm formation, growth and rupture has yet to be fully understood. Many factors seem to be relevant and several studies have been done trying to isolate the different factors and sometimes with contradictory results. The probable cause for the contradictory results is that a single quantity is not sufficient to determine whether or not an aneurysm will grow or rupture [5]. However, there are isolated factors that generally have been confirmed. Females and individuals in the age group 50-55 have a greater risk of developing aneurysms [21]. Smoking, hypertension and excessive alcohol intake are modifiable factors that lead to nearly doubling the risk of SAH [26]. Patients with the genetic disease Autosomal Dominant Polycystic Kidney Dis-

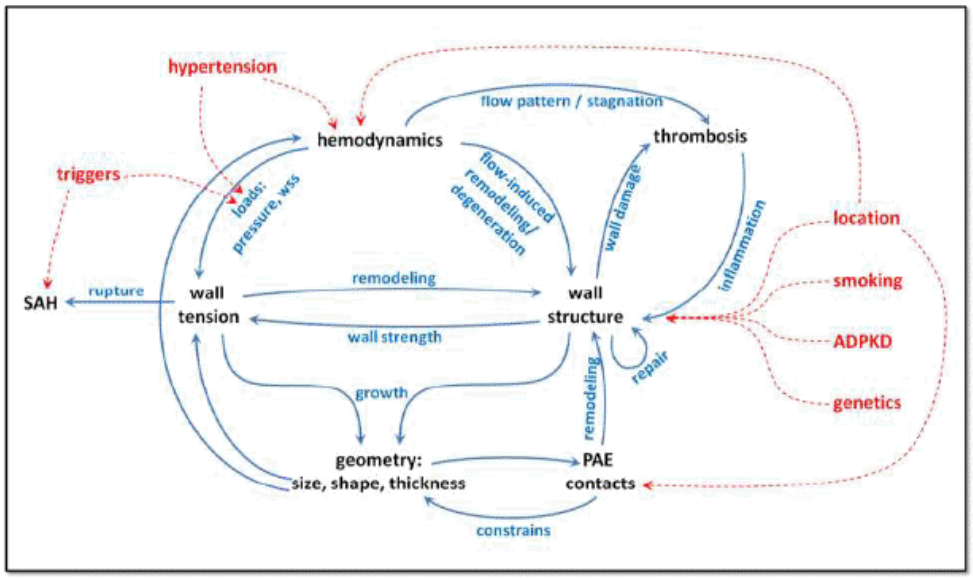

Figure 2.2: Factors that contributes to growth and rupture of aneurysms. Reprinted from Cebral and Raschi [5].

ease (ADPKD) have been reported to have five times more aneurysms than the general population [5]. The geometry(size and shape) of an aneurysm may contribute to the risk of rupture. A study found that if the aneurysm had an aspect ratio[2] higher than 1.6 they where much more likely to rupture [24]. The different factores are illustrated in Figure **??**.

2.1 Blood vessels and blood properties

A blood vessel is categorized into three layers. From inner to outer layer they are [13]:

- Tunica intima, consists of an innermost layer of endothelial cells and some connective tissue.
- Tunica media, consists of smooth muscle fibers with elastic fibers.
- Tunica adventita, consists of relatively loose connective tissue and nerve fibers.

[2]The ratio between the width and the height of a shape

The thickness of the layers varies throughout the cardiovascular system and the intracranial vessels generally have a thinner media compared to other vessels. Between the intima and media it exists an elastic membrane called the internal elastic lamina. In some parts of the cardiovascular system there exist an elastic membrane between the media and adventita as well. However, the intracranial blood vessels lack this membrane [10].

The aneurysm wall generally consists of a thicker intima, a fragmented or absent internal elastic lamina, a thin or absent layer of the media and an adventita that is the same as the parent vessel [2, 13]. Hence the wall is thinner, and is less responsive to hemodynamic forces.

The endothelial cells are elastic cells protecting the other layers of the blood vessel from the flowing blood [10]. These cells stretch with the WSS and become more ellipsoidal as WSS increase [7, 15]. If the WSS exceeds a critical limit the endothelial cells may get damaged and expose the hemodynamic forces to the other unprotected parts of the artery wall. This may lead to the formation of an aneurysm. This critical limit is different for every individual but endothelial cells have been observe to take damage when exposed to WSS magnitude of $40Pa$ [10].

Blood consists of plasma, red blood cells, white blood cells and platelets. While the latter two are important, they account for less than 2% off the volume. The distribution of the plasma and the red blood cells are approximately 55% plasma and 45% red blood cells. While plasma contains mostly water (92%) and behaves more or less like water, the red blood cells do not [14]. In large blood vessels the individual red blood cells are relatively small in volume, therefore the Newtonian assumption is valid. However, as vessels become smaller the non-Newtonian effects are more relevant. The arteries in the brain varies in size, but studies suggests that the effects of a non-Newtonian blood model is small compared to other variables [28]. We will model blood as a Newtonian fluid and as stated in Chapter 1 use a non-Newtonian model as a reference.

Chapter 3

Mathematical formulation

The Navier-Stokes equations is the equations governing gases and fluids in motion. It relates u, the velocity vector field, and p, the pressure field, of the fluid/gas. Parameters needed to solve this equation is ρ for the density of the fluid, and μ the dynamic viscosity. The equations will be used in this thesis to model the blood in motion within the arteries of the brain. The Navier-Stokes equations are derived from two basic principles, namely the conservation of mass and the conservation of momentum.

3.1 Derivation of Navier-Stokes equations for incompressible fluids

We consider the fluid to be a continuum. This means that we assume the mass to be continuous and to fill up the space it occupies completely.

For the derivation of the Navier-Stokes equations we need some notation and tools. Let $\Omega(t) \in \mathbb{R}^n$ be an arbitrarily chosen domain in the fluid that can change with time. The following theorem called Reynolds transport theorem is needed for the derivation.

Theorem 3.1. *Let $f : \Omega(t) \times [0, T] \to \mathbb{R}$ be a differentiable function. Then the following holds*

$$\frac{d}{dt} \int_{\Omega(t)} f(x,t)\, dx = \int_{\Omega(t)} \frac{\partial f(x,t)}{\partial t}\, dx + \int_{\partial\Omega(t)} f(x,t)(u \cdot n)\, dS.$$

Conservation of mass

At any given time the mass inside a volume should remain constant. This give rise to the equation

$$\frac{d}{dt}\int\limits_{\Omega(t)} \rho \, \mathrm{d}x = 0. \tag{3.1}$$

Use the transport theorem on (3.1) and get

$$\int\limits_{\Omega(t)} \frac{\partial \rho}{\partial t} \, \mathrm{d}x + \int\limits_{\partial\Omega(t)} \rho(u \cdot n) \, \mathrm{d}S = 0. \tag{3.2}$$

Transform the surface integral to a volume integral by Gauss/Greens theorem

$$\int\limits_{\partial\Omega(t)} \rho(u \cdot n) \, \mathrm{d}S = \int\limits_{\Omega(t)} (\nabla \cdot u)\rho + u \cdot \nabla\rho \, \mathrm{d}x. \tag{3.3}$$

Put this in equation (3.2)

$$\int\limits_{\Omega(t)} \frac{\partial \rho}{\partial t} + (\nabla \cdot u)\rho + u \cdot \nabla\rho \, \mathrm{d}x = 0. \tag{3.4}$$

Since $\Omega(t)$ is chosen arbitrarily the integrand must be equal to zero

$$\frac{\partial \rho}{\partial t} + (\nabla \cdot u)\rho + u \cdot \nabla\rho = 0. \tag{3.5}$$

Let us assume that the fluid is incompressible i.e. ρ is constant. Then the equation (3.5) gives

$$\nabla \cdot u = 0. \tag{3.6}$$

Conservation of momentum

Newtons second law of motion states that the change in linear momentum is equal to the force acting on the body. This gives the equation

$$\sum F = \frac{d}{dt}\int\limits_{\Omega(t)} \rho u \, \mathrm{d}x. \tag{3.7}$$

Use the transport theorem on (3.7) and get

$$\frac{d}{dt}\int\limits_{\Omega(t)} \rho u \, \mathrm{d}x = \int\limits_{\Omega(t)} \frac{\partial \rho u}{\partial t} \, \mathrm{d}x + \int\limits_{\partial\Omega(t)} \rho u(u \cdot n) \, \mathrm{d}S. \tag{3.8}$$

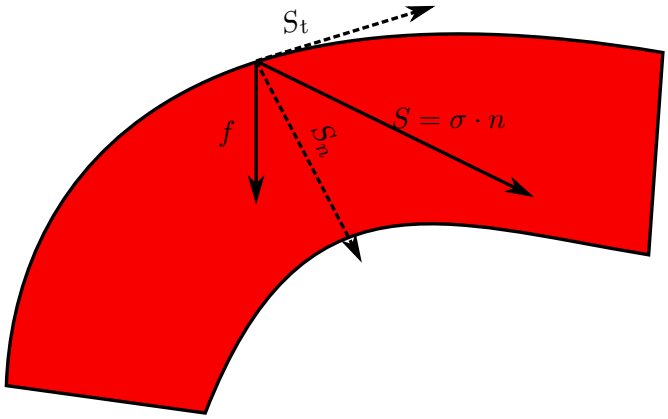

Figure 3.1: Forces on the artery wall. Body forces f is usually gravity. The arrows are not to scale.

Use the Gauss/Green theorem on the boundary term in (3.8) and assume an incompressible fluid

$$\frac{d}{dt}\int\limits_{\Omega(t)} \rho u \, \mathrm{d}x = \int\limits_{\Omega(t)} \rho\frac{\partial u}{\partial t} + \rho u(\nabla \cdot u) + \rho(u \cdot \nabla u) \, \mathrm{d}x. \tag{3.9}$$

Since we have an incompressible fluid $\nabla \cdot u = 0$ we are then left with

$$\frac{d}{dt}\int\limits_{\Omega(t)} \rho u \, \mathrm{d}x = \int\limits_{\Omega(t)} \rho\frac{\partial u}{\partial t} + \rho(u \cdot \nabla u) \, \mathrm{d}x. \tag{3.10}$$

The forces can be split into two forces: forces acting on the body f like gravity and forces acting on the surface of the body S (see Figure 3.1). The surface force can be written as $S = \sigma \cdot n$ where n is the inward pointing normal and σ is the stress tensor. The stress tensor varies with the velocity u and the pressure p. This leads to the equation

$$\sum F = \int\limits_{\Omega(t)} \rho f \, \mathrm{d}x + \int\limits_{\partial\Omega(t)} \sigma \cdot n \, \mathrm{d}S. \tag{3.11}$$

Use Gauss/Green again and transform the surface integral to a volume integral

$$\int\limits_{\partial\Omega(t)} \sigma \cdot n \, \mathrm{d}S = \int\limits_{\Omega(t)} \nabla \cdot \sigma \, \mathrm{d}x. \tag{3.12}$$

Using (3.10 - 3.12) and gathering all terms on one side gives

$$\int\limits_{\Omega(t)} \rho f + \nabla \cdot \sigma - \rho\frac{\partial u}{\partial t} - \rho(u \cdot \nabla u) \, \mathrm{d}x = 0. \tag{3.13}$$

Again since $\Omega(t)$ is an arbitrary domain the integrand must be zero hence the equation becomes

$$\rho\frac{\partial u}{\partial t} + \rho(u \cdot \nabla u) = \rho f + \nabla \cdot \sigma. \tag{3.14}$$

Given the incompressibility assumption, the stress tensor σ can be derived [14] as

$$\sigma = -pI + 2\mu\epsilon(u), \tag{3.15}$$

where $\epsilon(u)$ is the strain rate tensor given as the symmetric gradient

$$\epsilon(u) = \frac{1}{2}(\nabla u + \nabla u^T). \tag{3.16}$$

Inserting (3.15) into (3.14) gives

$$\frac{\partial u}{\partial t} + (u \cdot \nabla u) = f - \frac{1}{\rho}\nabla p + \nabla \cdot (2\frac{\mu}{\rho}\epsilon(u)). \tag{3.17}$$

The kinematic viscosity is defined as $\nu = \frac{\mu}{\rho}$. By using this viscosity we get

$$\frac{\partial u}{\partial t} + (u \cdot \nabla u) = f - \frac{1}{\rho}\nabla p + 2\nabla \cdot \nu\epsilon(u). \tag{3.18}$$

3.2 Boundary conditions

To get a unique solution of the equations it is necessary to have conditions on the boundary. We will preform simulations on patient specific geometries with aneurysms. As we are mainly interested in the flow in and around the aneurysm, we cut off the domain a distance away from it getting boundaries for the inflow and outflow as well as on the wall. The boundary can therefor be split into inflow boundaries $\partial\Omega_I$, outflow boundaries $\partial\Omega_O$ and artery wall boundaries $\partial\Omega_W$ (see Figure 3.2). The whole boundary $\partial\Omega$ can now be written as

$$\partial\Omega_I \cup \partial\Omega_O \cup \partial\Omega_W = \partial\Omega. \tag{3.19}$$

Wall boundary

In this thesis we will assume that the walls of the artery are stationary and stiff, known as the rigid-wall assumption. Rigid walls is clearly a simplification since arteries move around, stretches and contracts due to the forces of the blood flowing inside. Implementing elastic walls is possible. This would mean

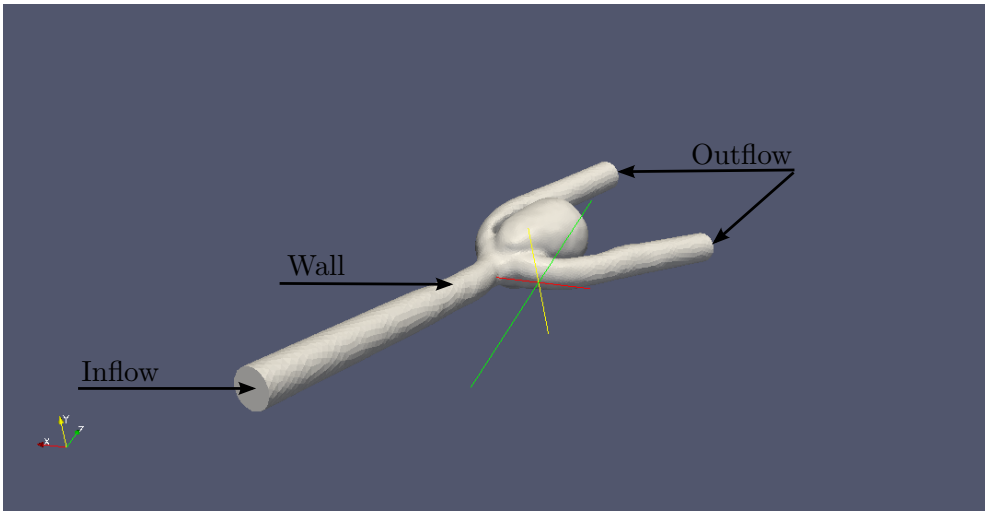

Figure 3.2: The different boundary conditions.

a fluid-structure interaction (FSI) model with parameters for the elasticity of the arteries. This would also be more computationally demanding which means that the computational error would be greater. Simulations done with a FSI model show that with rigid walls we may give some changes in flow pattern. It may also result in a higher WSS than what the FSI model predicts [23].

We will also assume that the velocity of the fluid relative to the boundary is zero and is known as the no-slip condition. It is a well known and tested condition. These two assumptions gives that the velocity is zero at the walls

$$u|_\Gamma = 0 \text{ for } \Gamma \in \Omega_W. \tag{3.20}$$

Inflow boundary

For the inflow we can prescribe a velocity u_I. We will use the solution of flow in a cylinder as the inflow profile. We do this because we have no prior information about the flow at the inflow boundary. This means we can not know how this profile should have been. However as the distance away from the cut-off increases the error in the assumption will decrease. This implies that if we choose the inflow artery to a sufficient length we minimize the possible error of this assumption.

We assume that the flow is laminar and fully developed. The cylinder laminar fully developed flow is called Poiseuille flow and we can find an exact solution.

This derivation of the exact solution is taken from Kundu et al. [14]. We use cylindrical coordinates (x, r, θ) and a cylinder with radius R letting x be the direction along the cylinder. Since we have laminar flow the velocity is only in the direction of the cylinder and since the flow is fully developed the velocity is only dependent of r

$$u = w(r)\mathbf{i}. \tag{3.21}$$

By using Newtonian fluid the Navier-Stokes equations can be written as

$$\frac{Du}{dt} = f - \frac{1}{\rho}\nabla p + \nu\Delta u \tag{3.22}$$

where $\frac{Du}{dt} = \frac{\partial u}{\partial t} + (u \cdot \nabla u)$ is called the material derivative, or the acceleration. Since a fully developed flow has no acceleration (3.22) becomes

$$-\frac{1}{\rho}\nabla p + \nu\Delta u = 0. \tag{3.23}$$

Using the Laplacian for cylindrical coordinates we get

$$-\frac{dp}{dx} + \mu\frac{1}{r}\frac{d}{dr}\left(r\frac{dw}{dr}\right) = 0 \tag{3.24}$$

$$\frac{\partial p}{\partial r} = \frac{\partial p}{\partial \theta} = 0. \tag{3.25}$$

We recognize p as only a function of x. Since w is a function of r the only way we can have (3.24) is when the two terms are constant. By rearranging equation (3.24) we get

$$\frac{d}{dr}\left(r\frac{dw}{dr}\right) = \frac{\partial p}{\partial x}\frac{r}{\mu}. \tag{3.26}$$

The solution to (3.26) is

$$w(r) = \frac{dp}{\mathrm{d}x}\frac{1}{4\mu}r^2 + A\ln(r) + B. \tag{3.27}$$

Since w need to be bounded we must have $A = 0$, and with the no-slip boundary condition $w(R) = 0$ we get the solution

$$w(r) = \frac{dp}{\mathrm{d}x}\frac{1}{4\mu}(r^2 - R^2). \tag{3.28}$$

We indentify the solution as a parabolic profile with magnitude $\frac{dp}{\mathrm{d}x}\frac{1}{4\mu}$. We will use this as our inflow condition

$$u_I = A(t)(R^2 - r^2)n \tag{3.29}$$

where R is the radius of the inflow artery, n the inward pointing normal and $A(t)$ is the magnitude of the inflow (see Figure 3.3).

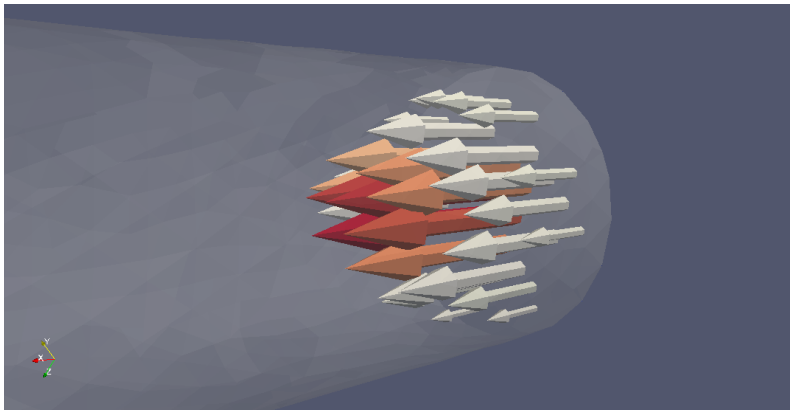

Figure 3.3: Parabolic inflow boundary condition.

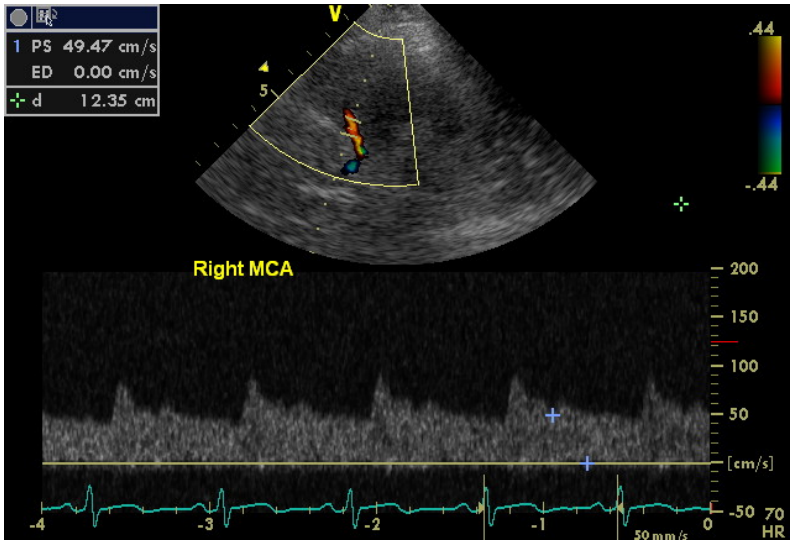

Figure 3.4: Doppler image of magnitude of flow in right MCA with 70 beats per minute.

The magnitude of the inflow can be measured by a Doppler echocardiography. It is a non-invasive procedure that examines the speed in which the blood flows for a specified artery. The echocardiography gives us an image (seen in Figure 3.4) of the speed of the blood in a specified vessel over several cardiac cycles. Given such images we extracted data points y_i for the speed and t_i for the time of the image for one cardiac cycle using a tool called *xyscan*. To get several cycles we repeated this cycle over again, assuming that the cycle does not change.

We use splines to create a continuous curve from the data points $A(t)$. To

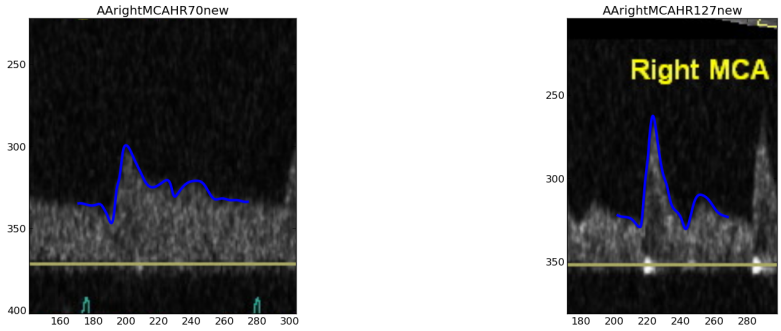

(a) HR 70 (b) HR 127

Figure 3.5: Curve fitted to Doppler images of right MCA for high and low heart rate.

Name	Heart rate $[beat/min]$	Average speed $[mm/s]$	Peak systole $[mm/s]$
Low	70	572	911
High	127	498	1139

Table 3.1: Properties of the inflow rates used in this thesis.

verify that the curve $A(t)$ approximates the magnitude of the given Doppler image well, the curve was plotted over the image and observed that it coincided with the image. In this thesis we will use the two curves produced by the images in Figure 3.5. We will refer to the two heart rates as *high* and *low* heart rate. Properties of the inflow rates can be viewed in Table 3.1. It would be preferable to use patient specific images but this data is not available.

An interesting property is that the average speed of the low heart rate is greater than the one for high heart rate. This will have implications for the results as the WSS are dependant on the inflow flux. Since we use a scaled parabolic inflow, the inflow flux can calculated by

$$Q = \int_{\partial\Omega_I} u_I \, \mathrm{d}S = \int_{\partial\Omega_I} A(t)(R^2 - r^2)n \, \mathrm{d}S = CA(t). \tag{3.30}$$

Hence the average inflow flux and WSS will be larger in the low heart rate compared to the high heart rate. The ratio between the average inflow flux between high and low heart rate will be

$$\frac{\overline{Q_h}}{\overline{Q_l}} = \frac{C\overline{A_h}}{C\overline{A_l}} = \frac{498}{572} = 0.87. \tag{3.31}$$

Outflow boundary

For the outflow arteries we will apply the Neumann condition for the velocity, meaning the normal derivative is zero ($\nabla u \cdot n = 0$). For simplicity, the homogeneous Dirichlet condition will be used on the pressure. Since the Navier-Stokes equations are only dependant on the gradient of the pressure, we need a Dirichlet condition to determine the pressure value. This condition is called the traction-free boundary condition.

3.3 Initial condition

The Navier-Stokes equations are time dependent, implying the need for an initial starting velocity and pressure for $t = 0$. The solution become less dependant on the condition set at $t = 0$ as the solution develops in time. Since it is easy and convenient to set zero as our initial condition we will do so, $u(x, 0) = 0$, $p(x, 0) = 0$. This satisfy the equations and is easily implemented. To make sure that the error in the initial condition is negligible we will run our simulations for three cardiac cycles before gathering the simulations at the fourth.

3.4 Wall shear stress computation

The wall shear stress can be computed from the forces on the surface of the domain. These forces are defined as

$$S = \sigma \cdot n \tag{3.32}$$

where n is the inward pointing normal. This can be decomposed into a normal and tangential component S_n and S_t (see Figure 3.1). We get the normal and tangential component by

$$S_n = (S \cdot n)n \qquad S_t = S - S_n. \tag{3.33}$$

The magnitude of the WSS will be denoted by τ.

$$\tau = \sqrt{S_t \cdot S_t}. \tag{3.34}$$

3.5 Viscosity, density and units

We need to pick the units for length, time and mass. The meshes provided will be in millimeter so this will be our unit of length. We pick gram as the unit for mass such that the unit for force per area will become the SI-Unit Pa (see Table 3.2a). The units of the computed values can be found in Table 3.2b.

Mostly we will model blood as a Newtonian fluid in this thesis i.e. the viscosity is constant. The constants for viscosity and density are found in academic literature [14] and provided in Table 3.2c. The non-Newtonian model we will use is a modified Cross model. It depends on the shear rate

$$\gamma = \sqrt{2\|\epsilon(u)\|_F} \tag{3.35}$$

where F denotes the Förbenius norm and is defined as [28]

$$\mu = \frac{\mu_0 - \mu_\infty}{(1 + (\lambda\gamma)^m)^a} + \mu_\infty. \tag{3.36}$$

The parameters are set to

$$\mu_0 = 0.056\frac{g}{smm} \quad \mu_\infty = 0.00345^1\frac{g}{smm} \quad \lambda = 3.736s \quad m = 2.406 \quad a = 0.254. \tag{3.37}$$

[1]There will be a small difference in the general viscosity between the Newtonian and non-Newtonian model. This because μ in the Newtonian case is not equal μ_∞. This was discovered late in the process and were not possible to correct.

Quantity	SI-Unit	Unit Used
Length	m-meter	mm-millimeter
Time	s-second	s-second
Mass	kg-kilogram	g-gram

(a) Units

Quantity	Notation	Unit
Velocity field	$u(x,t)$	$\frac{mm}{s}$
Pressure	$p(x,t)$	Pa
Wall shear stress	$\tau(x,t)$	Pa

(b) Computed

Quantity	Notation	Unit	Value
Dynamic viscosity	μ	$\frac{g}{smm}$	$3.2 \cdot 10^{-3}$
Density	ρ	$\frac{g}{mm}$	$1.054 \cdot 10^{-3}$
Kinematic viscosity	ν	$\frac{mm^2}{s}$	3.036

(c) Constants

Table 3.2: Units and values of computed quantities and constants.

3.6 Assumptions and final model

In the mathematical model we have made several assumptions. The assumptions made are listed as following:

- Blood behaves as a Newtonian fluid.
- Arteries are modelled as stationary and stiff.
- Blood has a constant density.
- Parabolic inflow profile.
- Homogeneous outflow conditions.
- Gravity is negligible.

The final problem description is stated in equations (3.38 - 3.41).

$$\left.\begin{aligned} u_t + u \cdot \nabla u &= -\frac{1}{\rho}\nabla p + 2\nabla \cdot \nu\epsilon(u) + f \\ \nabla \cdot u &= 0 \\ u(x,0) &= 0 \\ p(x,0) &= 0 \end{aligned}\right\} \text{ for } x \in \Omega \tag{3.38}$$

$$u(x,t) = 0 \text{ for } x \in \Omega_w \tag{3.39}$$

$$u(x,t) = u_I \text{ for } x \in \Omega_I \tag{3.40}$$

$$p(x,t) = 0 \text{ for } x \in \Omega_O \tag{3.41}$$

Chapter 4

Numerical formulation

The Navier-Stokes equation is a highly non-trivial problem to solve. Although it is an old problem, new schemes are continually developed to find better solutions more efficiently. The Incremental Pressure Correction Scheme (IPCS) will be used for the simulations of blood in this thesis. Using FEniCS, it is shown to have good accuracy and efficiency for a variety of different problems [18].

4.1 Weak formulation

In partial differential equations (PDEs) there are two common ways of describing the problem. They are called the strong and the weak form of the equations. The strong form is the classical PDE and can be formulated by a differential operator L and a source term f. The equation becomes:

Find $u \in V$ for a suitable function space V such that

$$Lu = f. \tag{4.1}$$

The weak form can be formulated by two functionals $a(u, v)$ and $l(v)$. The weak problem formulation is:

Find $u \in V$ such that

$$a(u, v) = l(v) \; \forall v \in \hat{V} \tag{4.2}$$

for suitable function spaces V and $\hat{V}$. It is always possible to go from the strong form to the weak form by simply multiplying with a test function

$v \in \hat{V}$ and integrating over the domain Ω in which the equation is defined

$$Lu = f \implies Lu \cdot v = f \cdot v \implies \int_\Omega Lu \cdot v \, \mathrm{d}x = \int_\Omega f \cdot v \, \mathrm{d}x. \tag{4.3}$$

Similarly if u is a solution of the strong form, it will also be a solution to the weak form. The opposite is however not necessarily true. Solutions of the weak form can have the property of weak derivatives hence the name *weak*. Weak derivatives is defined by using the property of integration by parts:

Definition 4.1. *A function u is said to have a weak derivative in direction i if for all $\phi \in C_0^\infty(\Omega)$ there exist a function $v_i \in L^1(\Omega)$ such that*

$$\int_\Omega u\phi_{x_i} \, dx = -\int_\Omega v_i\phi \, dx \tag{4.4}$$

v_i is referred to as u_{x_i} in the weak sense.

In other words, a function is said to have a weak derivative if it is differentiable up to measure of zero.

The property of weak derivatives gives rise to function spaces called a Sobolev spaces in which the solutions of the weak form will lie. We will only use one particular Sobolev space in this thesis, namely $W^{1,2}$ which is often denoted H^1.

Definition 4.2. *The Sobolev space $H^1(\Omega)$, $\Omega \in \mathbb{R}^n$, consists of functions $u : \Omega \to \mathbb{R}$ such that u_{x_i} exist and $u, u_{x_i} \in L^2(\Omega)$ for $i = 1, 2, ..., n$, where u_{x_i} is the derivative in the weak sense. The norm is defined as*

$$\|u\|_{H^1} = (\|u\|^2_{L^2(\Omega)} + \|\nabla u\|^2_{L^2(\Omega)})^{\frac{1}{2}}. \tag{4.5}$$

This can be defined for vector functions as well, by simply letting every component be a $H^1(\Omega)$ function

$$\mathbf{H}^1(\Omega) = \{u : \Omega \to \mathbb{R}^d | u_i \in H^1(\Omega) \text{ for } i = 1, 2, ..., d\}. \tag{4.6}$$

In this thesis we will only work in 2-D and 3-D so $d = 2, 3$.

4.2 Finite Element Method

In the field of PDEs we require a tool to discretize the equations into finite approximations of the real solution. The reason being that finding an analytical solution is in many cases hard and may often be impossible. Another

issue, regarding the Navier-Stokes equation, is that the existence of a solution is not shown. In this thesis the Finite Element Method (FEM) will be used to discretize the equations. The strengths of the FEM is how easy it is to adopt to different complex domains and solve equations over a mesh with varying cell size. These advantages allows us to simulate flow in different patient aneurysms and discretize the domain such that we get higher accuracy with less computational demand.

The Finite Element Method can be described with these steps:

- Identifying the weak form of the PDE.
- Discretize the domain and find a finite dimensional function space that is contained in the space where the solution of the equation lies.
- Defining a new problem from the weak form and the finite dimensional space. This problem will have finitely many degrees of freedom.
- Deriving an algorithm to find the degrees of freedom.

Using finite element the goal is to transform a infinite-dimensional problem into a finite dimensional one. This is done by choosing finite dimensional function spaces $V_h, \hat{V}_h$ such that they are subsets of the original function spaces

$$\dim(V_h),\ \dim(\hat{V}_h) < \infty \qquad V_h \subset V, \hat{V}_h \subset \hat{V}. \tag{4.7}$$

Using the weak form of the equation we can formulate a new problem:

Find $u_h \in V_h$ such that

$$a(u_h, v_h) = l(v_h)\ \forall v_h \in \hat{V}_h. \tag{4.8}$$

This is a problem with finitely many unknowns and is solvable. How to choose these finite dimensional spaces and what kind of basis functions to use for the function space is the trick in the FEM.

A finite element is defined as:

Definition 4.3. *Let*

- $K \subset \mathbb{R}^n$ *be a bounded closed set with nonempty interior and piecewise smooth boundary (the element domain),*
- $\mathcal{P}$ *be a finite-dimensional space of functions on* K *(the space of shape functions) and*

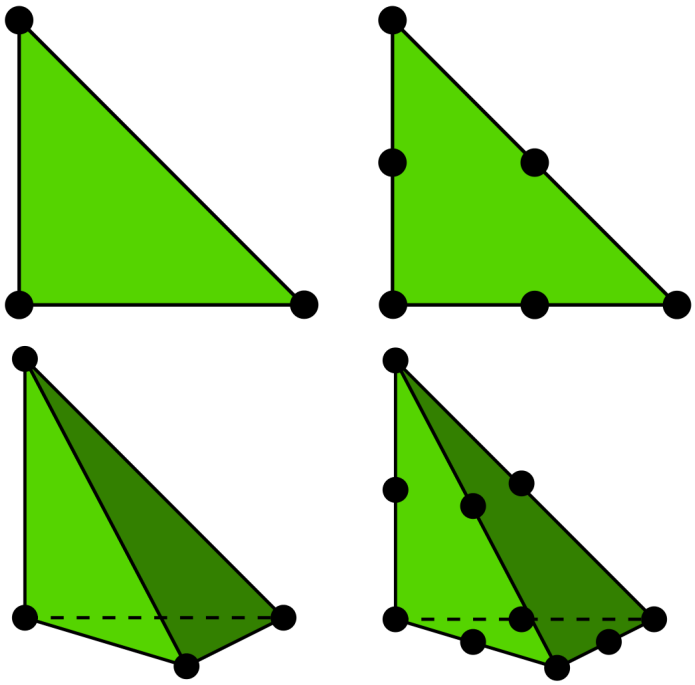

Figure 4.1: Nodes for langragian elements of degree 1 and 2 in 2D and 3D

- $\mathcal{N} = \{N_1, N_2, ..., N_k\}$ *be a basis for* $\mathcal{P}^*$ *(the set of nodal variables), where* $\mathcal{P}^*$ *denotes the dual space of* $\mathcal{P}$*.*

Then $(K, \mathcal{P}, \mathcal{N})$ *is called a finite element.*

Here K is usually a triangle in 2-D and a tetrahedron in 3-D. These elements defines our finite dimensional spaces. Elements come in many forms, but we will only use one type of element in this thesis, namely the Lagrangian elements.

Lagrangian elements of degree q is where the space of shape functions is q-degree polynomials and the set of nodal variables N_i is defined as

$$N_i(v) = v(x_i) \; \forall v \in \mathcal{P} \text{ for nodes } x_i \in K \text{ (see Figure 4.1).} \tag{4.9}$$

Another helpful definition is the one of the nodal basis. This will be the basis of our finite dimensional function space.

Definition 4.4. *Let* $(K, \mathcal{P}, \mathcal{N})$ *be a finite element. A basis* $\phi_1, \phi_2, \cdots, \phi_k$ *of* $\mathcal{P}$ *is called a nodal basis if* $N_i(\phi_j) = \delta_{ij}$ *for* $i, j = 1, 2, \cdots, k$*.*

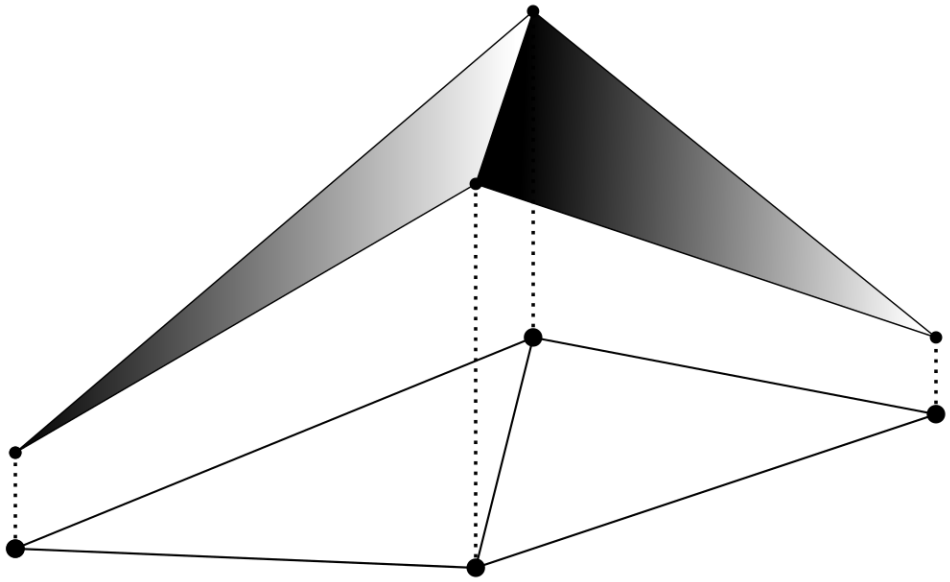

Figure 4.2: CG_1 function on 2D triangle mesh

Let us assume that the domain Ω can be discretized in a collections of element domains T

$$\bigcup_{K_i \in T} K_i = \Omega \tag{4.10}$$

and for simplicity, think of them as triangles. Glue together the Lagrangian elements and assure the common edges of two neighboring element domains have the same nodal variables. For every node x_i in the finite elements there will be a basis function ϕ_j. Using this we can then make a finite dimensional space

$$CG_q = \left\{ u_h : \Omega \to \mathbb{R} \middle| u_h = \sum_{j=1}^{n} U_j \phi_j \text{ for } U_j \in \mathbb{R} \right\}. \tag{4.11}$$

The way the Lagrangian elements are constructed the functions in CG_q will be piecewise q-degree polynomials on K_i and continuous over the domain Ω

$$CG_q = \left\{ u_h : \Omega \to \mathbb{R} | u_h \in C^0 \text{ and } u_h|_{K_i} \in P_q \text{ for } K_i \in T \right\} \tag{4.12}$$

Since the functions in CG_q are piecewise smooth functions and are glued together in a continuous matter, the measure of non-smoothness is zero. Hence CG_q is a subset of H^1. At this point we can use these function spaces as the

finite dimensional spaces in the weak formulation $V_h, \hat{V}_h = CG_q$ and (4.8) are reduced to:

Find $U_j \in \mathbb{R}$ such that

$$a(\sum_{j=1}^{n} U_j \phi_j, \phi_i) = l(\phi_i) \text{ for } i = 1, 2, \ldots, n. \tag{4.13}$$

This is a system of algebraic equations and can be solved by several methods. As we will see in this thesis $a(u, v)$ will be bilinear and we get a linear system to solve, hence (4.13) becomes a matrix vector equation

$$AU = b \tag{4.14}$$

where A and b are given as

$$A_{ij} = a(\phi_j, \phi_i) \qquad b_i = l(\phi_i). \tag{4.15}$$

In this thesis we use the linear elements CG_1 (see Figure 4.2). The reason being we would like the surface of our mesh to be as smooth as possible, hence we need more spatial grid points. This means that A becomes incredibly large and to get a solution in reasonable time, linear elements is the preferable choice.

4.3 Incremental Pressure Correction Scheme

The Incremental Pressure Correction Scheme (IPCS) is based on an operating splitting method. This means transforming the complicated Navier-Stokes equations, to a series of easy-to-solve equations. The first step is to neglect the incompressibility condition to get a tentative velocity, then use this computed velocity and correct it by ensuring that the final velocity is divergence free.

The discretization in time is done with backward Euler

$$\frac{\partial u}{\partial t}(t_{n+1}) \approx \frac{u^{n+1} - u^n}{\Delta t}. \tag{4.16}$$

Backward Euler is a good choice since we get a lower stability criterion on Δt, meaning we can take longer time steps without the solution blowing up and becoming unstable. By using backward Euler we implicitly assume laminar flow because the scheme dampens fluctuations in the solution.

Inserting (4.16) in the Navier-Stokes equations and evaluating the viscosity term $\nu := \nu(u^n)$ we get

$$u^{n+1} + \Delta t u^{n+1} \cdot \nabla u^{n+1} = -\frac{\Delta t}{\rho}\nabla p^{n+1} + 2\Delta t \nabla \cdot \nu\epsilon(u^{n+1}) + \Delta t f^{n+1} + u^n \tag{4.17}$$

$$\nabla \cdot u^{n+1} = 0. \tag{4.18}$$

The non-linearity $u^{n+1} \cdot \nabla u^{n+1}$ can be dealt with in several ways, but in this thesis we will linearize the term by $u^n \cdot \nabla u^{n+1}$. The equation then becomes

$$u^{n+1} + \Delta t u^n \cdot \nabla u^{n+1} = -\frac{\Delta t}{\rho}\nabla p^{n+1} + 2\Delta t \nabla \cdot \nu\epsilon(u^{n+1}) + \Delta t f^{n+1} + u^n \tag{4.19}$$

The tentative velocity is calculated by evaluating ∇p as the previous computed value, and neglecting the incompressibility condition. It will be denoted by u^*

$$u^* + \Delta t u^n \cdot \nabla u^* = -\frac{\Delta t}{\rho}\nabla p^n + 2\Delta t \nabla \cdot \nu\epsilon(u^*) + \Delta t f^{n+1} + u^n. \tag{4.20}$$

We impose the same boundary condition on u^* as we would on u^{n+1}.

Let $u^s = u^{n+1} - u^*$. Then subtracting equation (4.20) from (4.19) we get

$$u^s + q(u^s) = -\frac{\Delta t}{\rho}\nabla\phi \tag{4.21}$$

$$\nabla \cdot u^s = -\nabla \cdot u^* \tag{4.22}$$

where $q(u^s) = \Delta t(u^n \cdot \nabla u^s - 2\nabla \cdot \nu\epsilon(u^s))$ and $\phi = p^{n+1} - p^n$. We now neglect the q term from the equation which is an $O(\Delta t)$ approximation. Multiplying (4.21) with ∇ and using (4.22)

$$\frac{\Delta t}{\rho}\Delta\phi = \nabla \cdot u^* \tag{4.23}$$

we get a Poisson problem for ϕ.

After solving this mixed system we can update the new velocity and pressure explicitly

$$u^{n+1} = u^* - \frac{\Delta t}{\rho}\nabla\phi \tag{4.24}$$

$$p^{n+1} = \phi - p^n. \tag{4.25}$$

To summarize the IPCS we

- Solve u^* according to equation (4.20).
- Solve ϕ according to equation (4.23).
- Update u^{n+1} and p^{n+1} according to (4.24) and (4.25).

The weak form of IPCS

The IPCS can now be transformed into a weak form, with the purpose of using finite elements to solve the equations. The equation for the tentative velocity is

$$u^* + \Delta t u^n \cdot \nabla u^* = -\frac{\Delta t}{\rho}\nabla p^n + 2\Delta t \nabla \cdot \nu\epsilon(u^*) + \Delta t f^{n+1} + u^n. \tag{4.26}$$

Multiplying with a test function v and integrating over the domain Ω gives

$$\begin{aligned}(u^*, v)_\Omega + \Delta t\,(u^n \cdot \nabla u^*, v)_\Omega - 2\Delta t\,(\nabla \cdot \nu\epsilon(u^*), v)_\Omega = \\ - \frac{\Delta t}{\rho}\,(\nabla p^n, v)_\Omega + \Delta t\left(f^{n+1}, v\right)_\Omega + (u^n, v)_\Omega\,.\end{aligned} \tag{4.27}$$

Let $a_1(u^*, v)$ be the right hand side and $L_1(v)$ be the left hand side. Doing an integration by parts lets us search for a solution in a less strict space

$$(\nabla \cdot \nu\epsilon(u^*), v)_\Omega = \int_\Omega (\nabla \cdot \nu\epsilon(u^*)) \cdot v \,\mathrm{d}x \tag{4.28}$$

$$= -\int_\Omega \nu\epsilon(u^*) : \nabla v \,\mathrm{d}x + \int_{\partial\Omega} \nu\epsilon(u^*) n \cdot v \,\mathrm{d}S \tag{4.29}$$

$$= -\int_\Omega \nu\epsilon(u^*) : \nabla v \,\mathrm{d}x + \frac{1}{2}\int_{\partial\Omega} \nu\nabla u^* n \cdot v \,\mathrm{d}S + \frac{1}{2}\int_{\partial\Omega} \nu(\nabla u^*)^T n \cdot v \,\mathrm{d}S. \tag{4.30}$$

The test function v is defined such that v is zero on the part of the boundary where Dirichlet boundary condition are imposed. Hence the term $\nabla u^* n \cdot v$ is equal to zero on the whole boundary. Using this and (4.30), $a_1(u^*, v)$ becomes

$$\begin{aligned}a_1(u^*, v) = (u^*, v)_\Omega + \Delta t\,(u^n \cdot \nabla u^*, v)_\Omega \\ + 2\Delta t\,(\nu\epsilon(u^*), \nabla v)_\Omega - \Delta t\left(\nu(\nabla u^*)^T n, v\right)_{\partial\Omega}\,.\end{aligned} \tag{4.31}$$

For L_1 we get

$$L_1(v) = -\frac{\Delta t}{\rho}\,(\nabla p^n, v)_\Omega + \Delta t\left(f^{n+1}, v\right)_\Omega + (u^n, v)_\Omega \tag{4.32}$$

$$= \frac{\Delta t}{\rho}\,((p^n, \nabla \cdot v)_\Omega - (p^n v, n)_{\partial\Omega}) + \Delta t\left(f^{n+1}, v\right)_\Omega + (u^n, v)_\Omega \tag{4.33}$$

Using Korn's inequality it can be proven that there exists a unique solution to the problem $a_1(u, v) = L_1(v)$.

Multiplying the pressure equation with a test function q and integrating gives

$$(\Delta\phi, q)_\Omega = \frac{\rho}{\Delta t} (\nabla \cdot u^*, q)_\Omega \tag{4.34}$$

Integration by parts of the Laplace term gives

$$\begin{aligned} (\Delta\phi, q)_\Omega &= -(\nabla\phi, \nabla q)_\Omega + (\nabla\phi, qn)_{\partial\Omega} && (4.35)\\ &= -(\nabla\phi, \nabla q)_\Omega - \frac{\rho}{\Delta t} (u^s, qn)_{\partial\Omega} && (4.36) \end{aligned}$$

From the definition of u^s we have that $u^s|_{\Omega_W \cup \Omega_I} = 0$. For the pressure we have Dirichlet conditions on Ω_O hence $q|_{\Omega_O} = 0$. This implies that $u^s \cdot qn = 0$ on the whole boundary, hence $(u^s, qn)_{\partial\Omega} = 0$. The pressure equation can now be written as

$$(\nabla\phi, \nabla q)_\Omega = -\frac{\rho}{\Delta t} (\nabla \cdot u^*, q)_\Omega . \tag{4.37}$$

Existence and uniqueness of the Poisson equation is well known.

Chapter 5

Proper Orthogonal Decomposition

Proper Orthogonal Decomposition (POD) is a method for decomposing a time-varying function $u(x,t)$ into an orthonormal basis in space $u_i(x) \in L^2$ and orthogonal time coefficients $a_i(t)$

$$u(x,t) = \sum_{i}^{N} a_i(t) u_i(x). \tag{5.1}$$

In this thesis we have discretized the temporal domain and have a collection of vector functions $\{u^n \in \mathbf{CG_q}\}$ for $n = 1, 2, \cdots, M$ representing the velocity field at time t_n. We will do a discretized version of POD such that $\{u^n\}$ can be written as an orthonormal basis $\{\theta_i \in \mathbf{CG_q}\}$ and orthogonal coefficients $\{a_i^n\}$

$$u^n = \sum_{i=1}^{M} a_i^n \theta_i \tag{5.2}$$

$$(\theta_i, \theta_j)_\Omega = \delta_{ij} \qquad a_i \cdot a_j = |a_i| \delta_{ij}. \tag{5.3}$$

The POD basis is constructed in such a way that it is the *best* basis for $\{u^n\}$ in the L^2 norm.

Definition 5.1. *The best basis $\{\theta_i\}$ with coefficients $\{a_i^n\}$ of a collection of functions $\{u^n\}$ is such that for any other basis $\{\psi_i\}$ and coefficients $\{b_i^n\}$ we have*

$$\frac{1}{M} \sum_{n=1}^{M} \|u^n - \sum_{i=1}^{k} a_i^n \theta_i\|^2 \leq \frac{1}{M} \sum_{n=1}^{M} \|u^n - \sum_{i=1}^{k} b_i^n \psi_i\|^2 \tag{5.4}$$

for all $k \in \{1, 2, \cdots, N\}$, for some norm $\|\cdot\|$.

The POD can be viewed as finding the best basis for portraying the kinetic energy of a collection of velocity fields. Basis function θ_i and the coefficients a_i^n are often called mode number i.

5.1 Derivation of method

The problem of finding these basis functions can be set up as a calculus of variation problem [8]:

Find the extrema of the functional

$$J(\theta) = \sum_{n}^{M} |\left(u^n, \theta\right)_\Omega|^2 - \lambda(\|\theta\|^2_{L^2(\Omega)} - 1). \tag{5.5}$$

A necessary condition for the extrema is that the functional derivative is zero

$$\frac{d}{d\delta} J(\theta + \delta\psi)\big|_{\delta=0} = 0 \tag{5.6}$$

for an arbitrary function $\psi \in L^2$. This can be reduced to an eigenvalue problem

$$\int_\Omega \frac{1}{M} \sum_{n=1}^{M} u^n(x)(u^n(y) \cdot \theta_i(y))\, \mathrm{d}y = \lambda_i \theta_i(x). \tag{5.7}$$

The eigenfunctions of this problem are orthogonal [16]. We want to have a discrete eigenvalue problem to solve. By transforming the problem into an eigenvalue problem for the coefficient $\{a_i^n\}$, this is exactly what is obtained. Rearranging (5.7), we get

$$\frac{1}{M} \sum_{n=1}^{M} u^n \left(u^n, \theta_i\right)_\Omega = \lambda_i \theta_i. \tag{5.8}$$

Multiply with u^m and integrate over Ω

$$\frac{1}{M} \sum_{n=1}^{M} \left(u^n, u^m\right)_\Omega \left(u^n, \theta_i\right)_\Omega = \lambda_i \left(u^m, \theta_i\right)_\Omega. \tag{5.9}$$

The orthogonality of $\{\theta_i\}$ implies that $\left(u^n, \theta_i\right)_\Omega = \|\theta_i\|^2_{L^2(\Omega)} a_i^n$, hence we get

$$\frac{1}{M} \sum_{n=1}^{M} C_{mn} a_i^n = \lambda_i a_i^m \tag{5.10}$$

for $C_{mn} = (u^m, u^n)_\Omega$. Arranging this into a vector matrix equation we get the desired eigenvalue problem for a_i

$$\frac{1}{M} C a_i = \lambda_i a_i. \tag{5.11}$$

The matrix C is symmetric, hence the eigenvalues are real and non-negative and the eigenvectors are orthogonal. The numbering of the basis will come from the eigenvalues and will be from largest to smallest

$$\lambda_1 \geq \lambda_2 \geq \cdots \geq \lambda_r > 0. \tag{5.12}$$

In order for $\{\theta_i\}$ to be an orthonormal basis, as was the goal, we need to scale the eigenvectors such that

$$a_i \cdot a_i = M\lambda_i \tag{5.13}$$

and compute the basis with the scaling

$$\theta_i = \frac{1}{M\lambda_i} \sum_{n=1}^{M} a_i^n u^n \text{ for i=1,2,...,r.} \tag{5.14}$$

5.2 Properties of POD

Since the POD basis is the best basis (see Definition 5.1), the first modes will contain the main part of the flow. This gives a low-dimensional basis for the flow. Investigating how the velocity field is decomposed for different heart rates will help us gain knowledge of the differences that occur.

The amount of modes needed to express the velocity field may be a good indicator of the complexity of the flow. For a non-complex flow we might assume that the first mode will dominate the other modes. This is investigated in Section 7.3.

The orthogonality of the basis is a useful property when working with the modes, as it makes it possible to calculate measures of the different modes without having to find the basis itself

$$\|a_i^n \theta_i\|^2_{L^2(\Omega)} = (a_i^n)^2. \tag{5.15}$$

Also the norm of a POD approximation up to k can easily be computed by

$$\|\sum_{i=1}^{k} a_i^n \theta_i\|^2_{L^2(\Omega)} = \left(\sum_{i=1}^{k} a_i^n \theta_i, \sum_{i=1}^{k} a_i^n \theta_i \right)_\Omega = \sum_{i=1}^{k} (a_i^n)^2. \tag{5.16}$$

Chapter 6

Verification

When we do numerical computations of PDEs it is important to verify that the numerical schemes are correctly implemented. One way of verifying the solver is to find the exact solution to the problem. Then observe that the computed numerical solution converge to the exact solution when the discretization parameters tend to zero. There are several methods to find an exact solution and in this thesis we will use a method called manufactured solution.

6.1 Manufactured solution

The manufactured solution method follows these steps.

- Choose a velocity and a pressure and insert this into the governing equations.
- Calculate the body force term f.
- Insert this f into the solver

If the solver is correct, it should reproduce the chosen velocity and pressure. The chosen pressure and velocity will have to fulfill the boundary conditions and the divergence free condition. For this test we will consider a 2-D channel domain with length L in the x-direction and radius R. The corresponding meshes will have uniform cell size.

We choose the pressure and the velocity to be

$$u(x,y,t) = v(y,t)\mathbf{i} = Ae^{at}\sin\left(\frac{\pi n y}{R}\right)\mathbf{i} \tag{6.1}$$

$$p(x,y,t) = q(x,t) = -\sin(8\pi t)x. \tag{6.2}$$

For this choice of velocity the no-slip boundary condition is fulfilled and $\nabla\cdot u = 0$. The pressure is chosen such that the sine function has four cycles in the domain $t \in [0,1]$. The pressure gives the boundary conditions on the inflow $p(0,y,t)$ and the outflow $p(L,y,t)$. Now we can calculate f using the Navier-Stokes equations

$$f = \left((v_t - \nu v_{yy}) + \frac{1}{\rho}\frac{\partial p}{\partial x}\right)\mathbf{i} \tag{6.3}$$

$$= \left(\left(a + \frac{\nu\pi^2 n^2}{R^2}\right)Ae^{at}\sin\left(\frac{\pi n y}{R}\right) - \frac{1}{\rho}\sin(8\pi t)\right)\mathbf{i} \tag{6.4}$$

The constants have been varied to ensure that the same result is obtained for different values of the constants. In the results given, the constants are set to

$$A = 1.3 \qquad a = -0.1 \qquad n = 2 \qquad R = 2 \qquad L = 4. \tag{6.5}$$

The error is usually expressed as a functional of the quantity we wish to examine. We want the functional to be chosen such that it captures any sort of error that might be present. We will use the L^2 measure as our functional

$$E = \|(u_h - u_e)|_{t=T}\|_{L^2(\Omega)} \tag{6.6}$$

where u_h is the approximated solution by the solver and u_e is the exact solution. The error is calculated by interpolation of u_e onto CG_4 and using this as the exact solution. This measure of error captures whether the magnitude or the direction of the velocity field is correct over the whole domain.

To investigate the convergence rate we do a numerical experiment. We make an ansatz that the error is on the form

$$E = C\Delta t + Dh^r \tag{6.7}$$

where C and D are constants, h is the circulumradius[1] of a triangle in the mesh and $r \in (0,N]$ for a finite $N \in \mathbb{R}$. This is a fair assumption since the IPCS neglects a term of order Δt and the discretization in time is of first order.

Let j be an integer. By choosing the mesh such that $h = A2^{-j}$ and $\Delta t = B2^{-rj}$ we should expect the error to be decreasing with 2^{-jr} as j increases, or put in another way $E_j 2^{rj} = C$ for a constant C. So to find r we can plot $E_j 2^{rj}$ for different values of r and observe which plots that converges to a constant. We did this in Figure 6.1, and we can see that $r \approx 2$.

[1]The circulumradius is the radius of a sphere to which the whole triangle can be inscribed

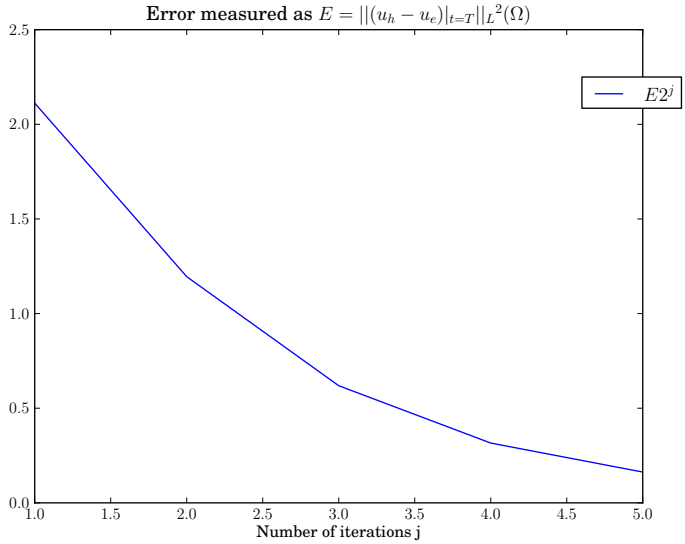

(a) Convergence plot for $r = 1$.

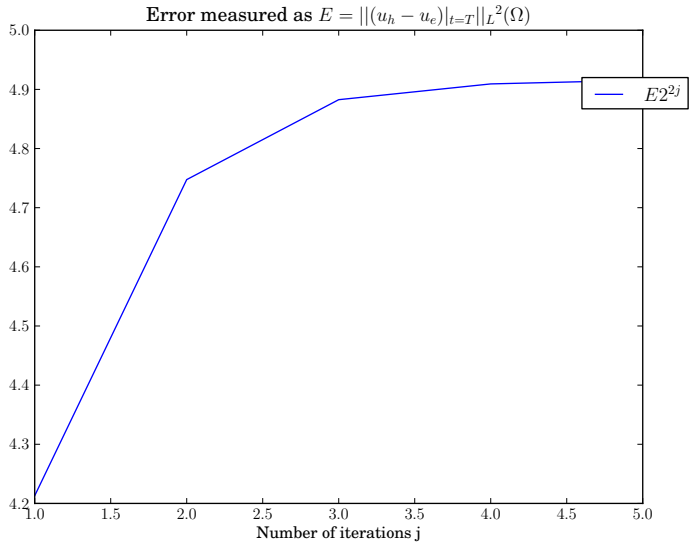

(b) Convergence plot for $r = 2$.

Figure 6.1: Plots of $E_j 2^{rj}$ for $r = 1$ and $r = 2$.

Given that a normal Poisson problem has a convergence rate of h^2 with linear elements one might assume that the convergence rate should be in the same region. Hence we can say with some confidence that our solver is correct.

6.2 WSS verification

To check the stress calculations we can compute the analytical solution of the wall shear stress. This serves as a double confirmation that the solver works as the WSS is a functional of the velocity field. To compute the WSS we first look at the wall $y = -R$ such that $\mathbf{n} = \mathbf{j}$ and compute the stress.

$$S = \sigma\mathbf{n} = \mu(\nabla u + \nabla u^T)\mathbf{n} - p\mathbf{n} \tag{6.8}$$

$$= \mu\frac{\partial u}{\partial y}|_{y=-R}\mathbf{i} - p|_{y=-R}\mathbf{j}. \tag{6.9}$$

From this we can find the WSS

$$\tau|_{y=-R} = |S_t|_{y=-R} = \mu|\frac{\partial u}{\partial y}\mathbf{i}|_{y=-R} \tag{6.10}$$

$$= \mu\frac{\pi n}{R}|Ae^{at}\cos\left(\frac{\pi n y}{R}\right)|_{y=-R} = \mu\frac{\pi n}{R}|A|e^{at} \tag{6.11}$$

Similarly the WSS at the wall $y = R$ is

$$\tau|_{y=R} = \mu\frac{\pi n}{R}|A|e^{at}. \tag{6.12}$$

To meassure the error we take the average of the WSS in the middle of the domain to test against the analytical expression for the WSS

$$E = \frac{|\tau_e - \tau_h|}{\tau_e}. \tag{6.13}$$

We measured the error with the same mesh parameters as in the numerical experiment in Section 6.1 with $r = 2$. The result viewed in Figure 6.2 shows the computed WSS tends to the exact WSS as the h and Δt tends to zero and we conclude that the stress calculations are correct.

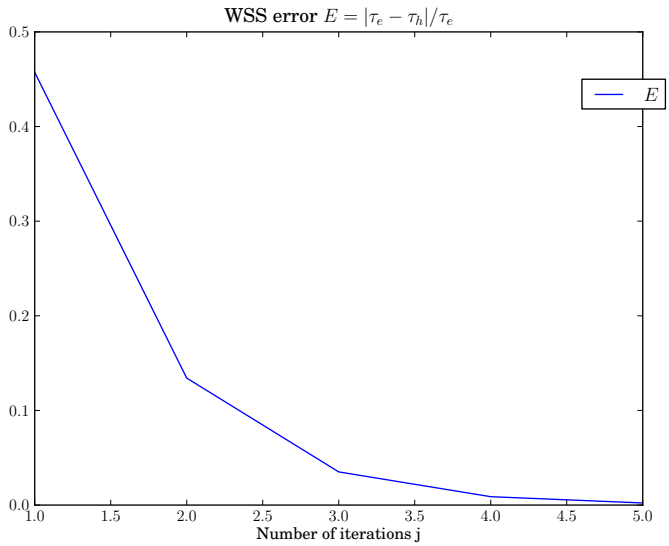

Figure 6.2: Error of WSS as h and Δt tends to zero.

Chapter 7

Qualitative results

This chapter presents ideas, results and the preparation upon which the rest of the research in this thesis is based on.

We have used one aneurysm to investigate how the flow and the WSS changes for high and low heart rate. Blood was modeled as a Newtonian fluid with the parameters presented in Table 3.2c. As inflow rates we used the two different heart rates discussed in Section 3.2. These can be seen in Figure 7.1 with the marked points systole, early diastole, middle diastole and end diastole.

The results that span over time was mapped to $t = [0, 1]$ making the time scale one cardiac cycle. We do this to easier compare high and low heart rate. The ParaView visualization tool was used for all the images involving the flow or the WSS. For both simulations 100 velocity fields were stored over one cardiac cycle to use for post-processing.

7.1 Convergence

First of all the parameters for the time stepping and mesh size must be chosen. To find suitable values for these parameters we did four simulations with different values of time steps and cell size. The simulations will be referred to as cases *a-d*. If the flow converges in some of these cases the parameters are sufficient to continue an analysis. The parameters are presented in Table 7.1.

To view the convergence we used the slice tool in ParaView which displays the magnitude of the flow in a 2-D plane (see Figure 7.2). This was done at

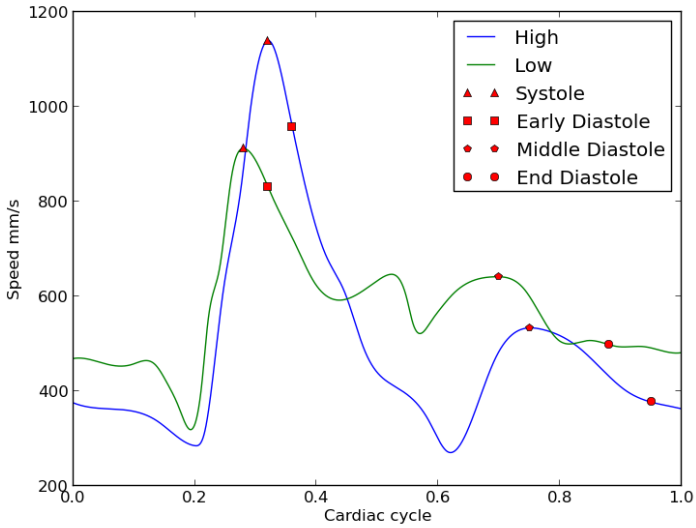

Figure 7.1: Cardiac cycles for high and low heart rate, mapped to $[0, 1]$.

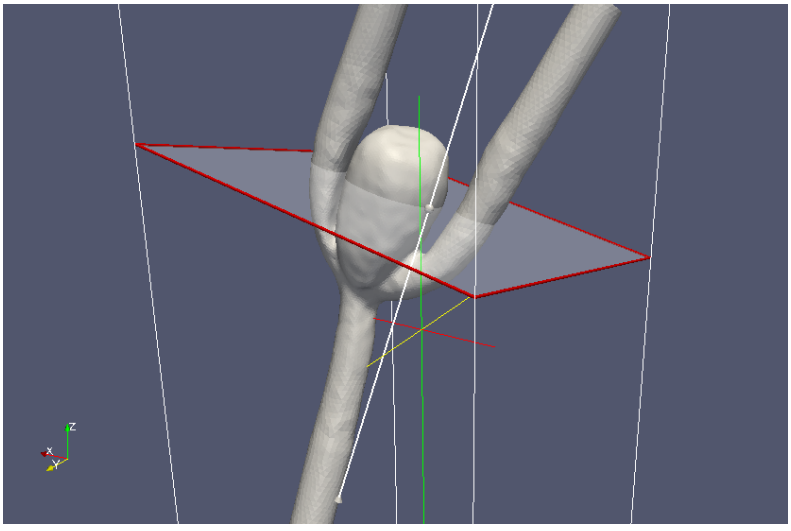

Figure 7.2: Plane used to conclude convergence.

Case	a	b	c	d
Time steps	800	2000	4000	8000
Number of cells	97000	267000	525000	1027000

Table 7.1: Convergence test cases.

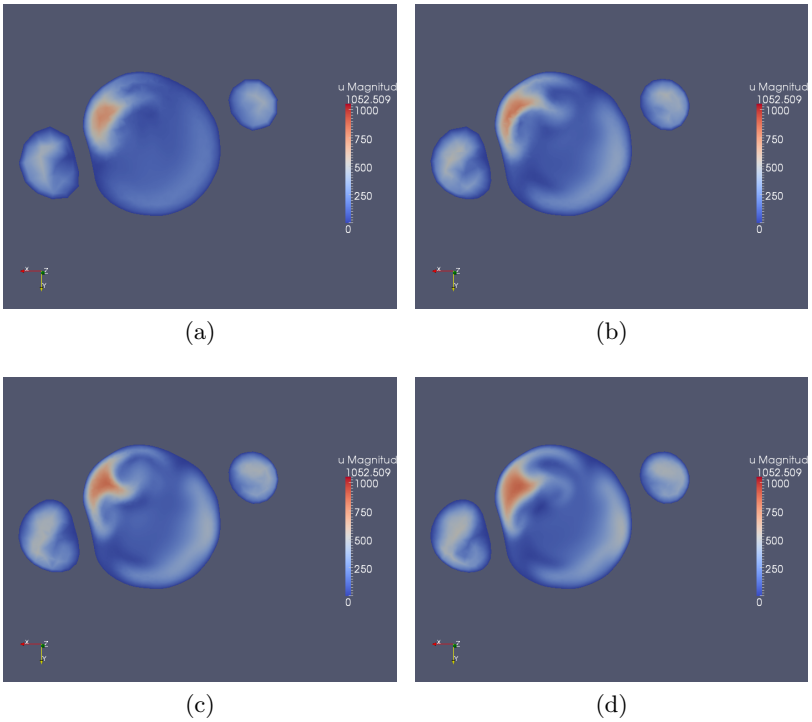

(a) (b)

(c) (d)

Figure 7.3: Convergence of flow. Simulations are done with the parameters given in Table 7.1.

systole time and is shown in Figure 7.3. Case c and d are similar. They are not identical but they portray the same features which is good enough for this purpose. The conclusion is that the flow does not change considerably between c and d, hence a sufficient range of time steps is $4000 - 8000$ and a sufficient range of the mesh size is $525000 - 1027000$ cells. For the rest of this chapter the simulations with case d parameters have been used.

7.2 Simulations

The velocity fields for high and low heart rate are visualized in Figure 7.4 and 7.5. We can see a difference in the magnitude of the flow between the two heart rates. This is expected since the speed of the inflow varies. In the high heart rate case we can see noticeable changes in the pattern at early and middle diastole.

The WSS magnitude for the different heart rates can be viewed in Figure 7.6 and 7.7. At systole and early diastole we see an overall higher WSS in the high heart rate case. The opposite is true for the middle and end of diastole. There are some changes in the distribution of the WSS for the two heart rates. At early diastole there are larger areas with high WSS in the high heart rate case. At the middle diastole the WSS pattern changes in the high heart rate from the right side to the left side, which is not observed in the low heart rate. This is visualized with a red circle. The region with highest WSS is at the apex of the aneurysm and has not changed with the higher heart rate.

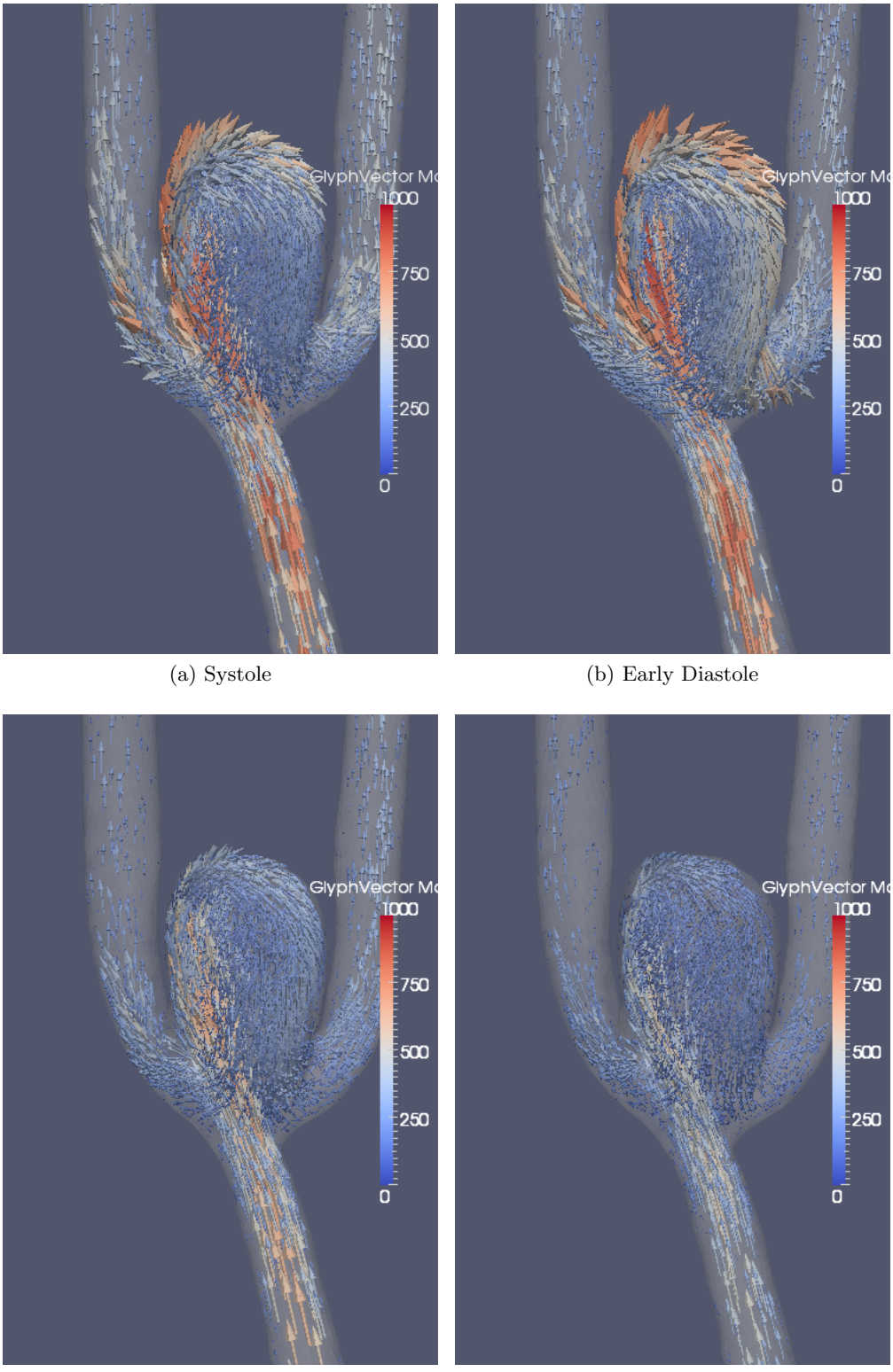

(a) Systole

(b) Early Diastole

(c) Middle Diastole

(d) End Diastole

Figure 7.4: The velocity field for different parts of the low heart rate cardiac cycle.

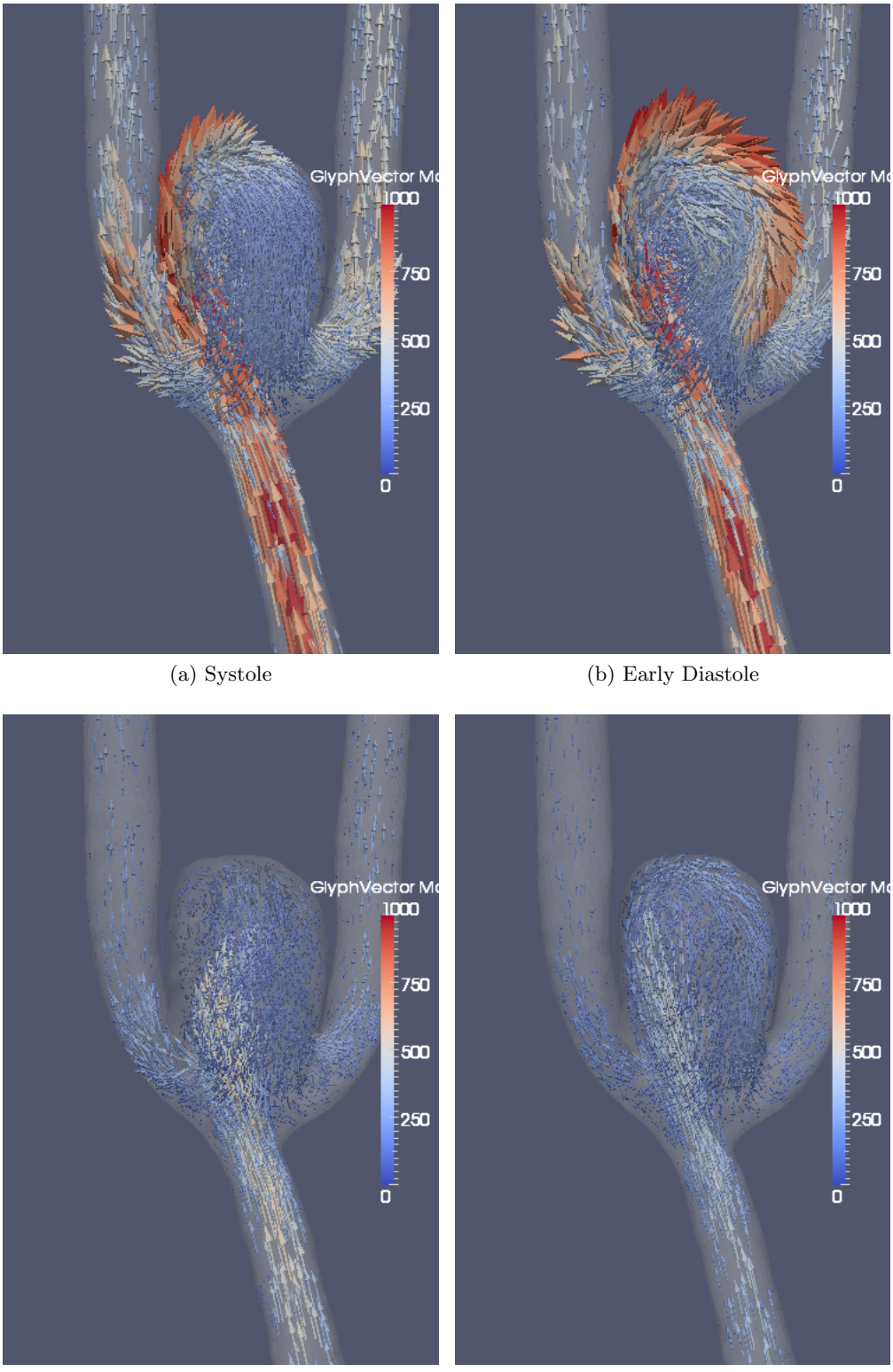

(a) Systole

(b) Early Diastole

(c) Middle Diastole

(d) End Diastole

Figure 7.5: The velocity field for different parts of the high heart rate cardiac cycle.

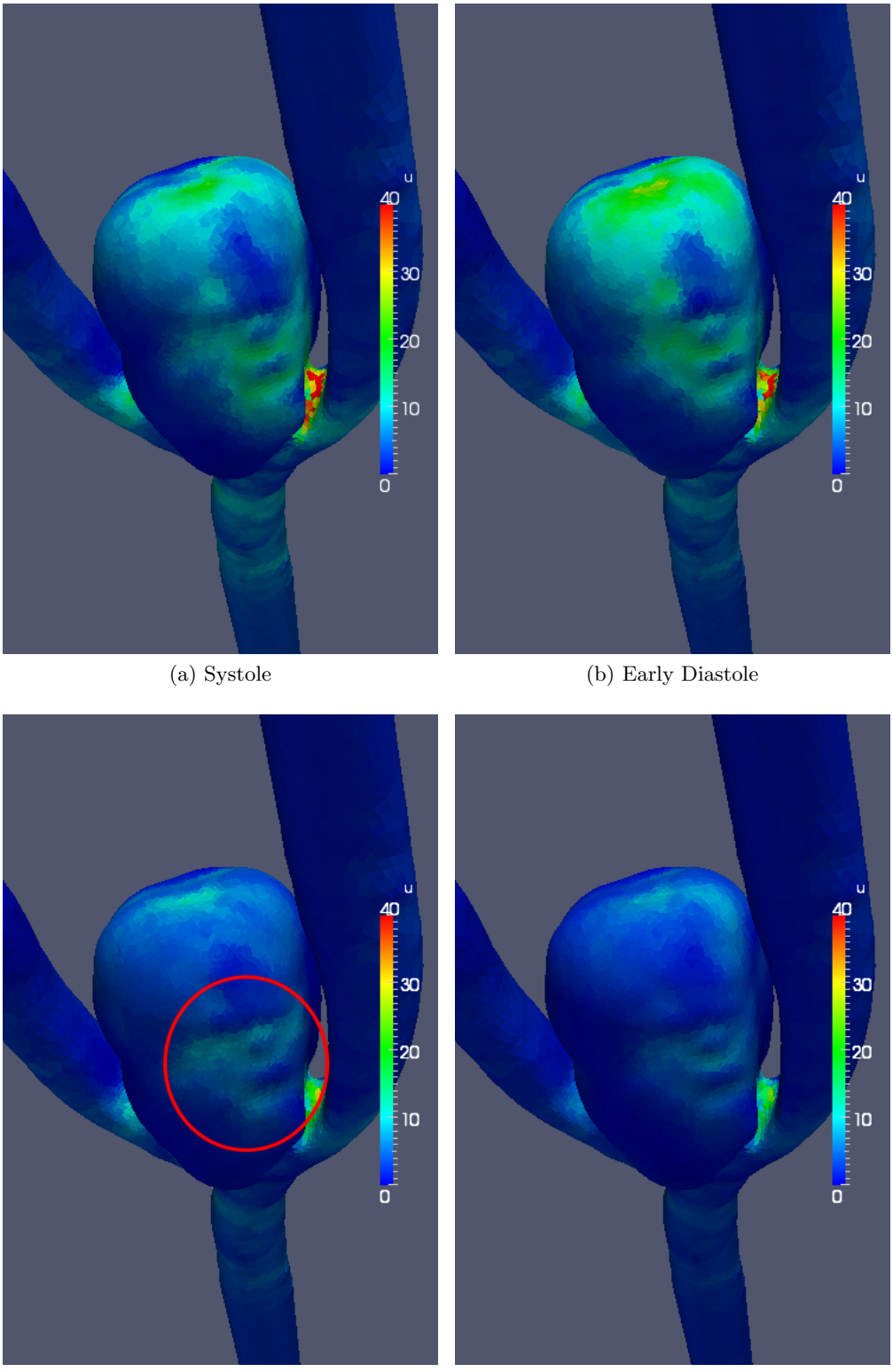

(a) Systole

(b) Early Diastole

(c) Middle Diastole

(d) End Diastole

Figure 7.6: The WSS for different parts of the low heart rate cardiac cycle.

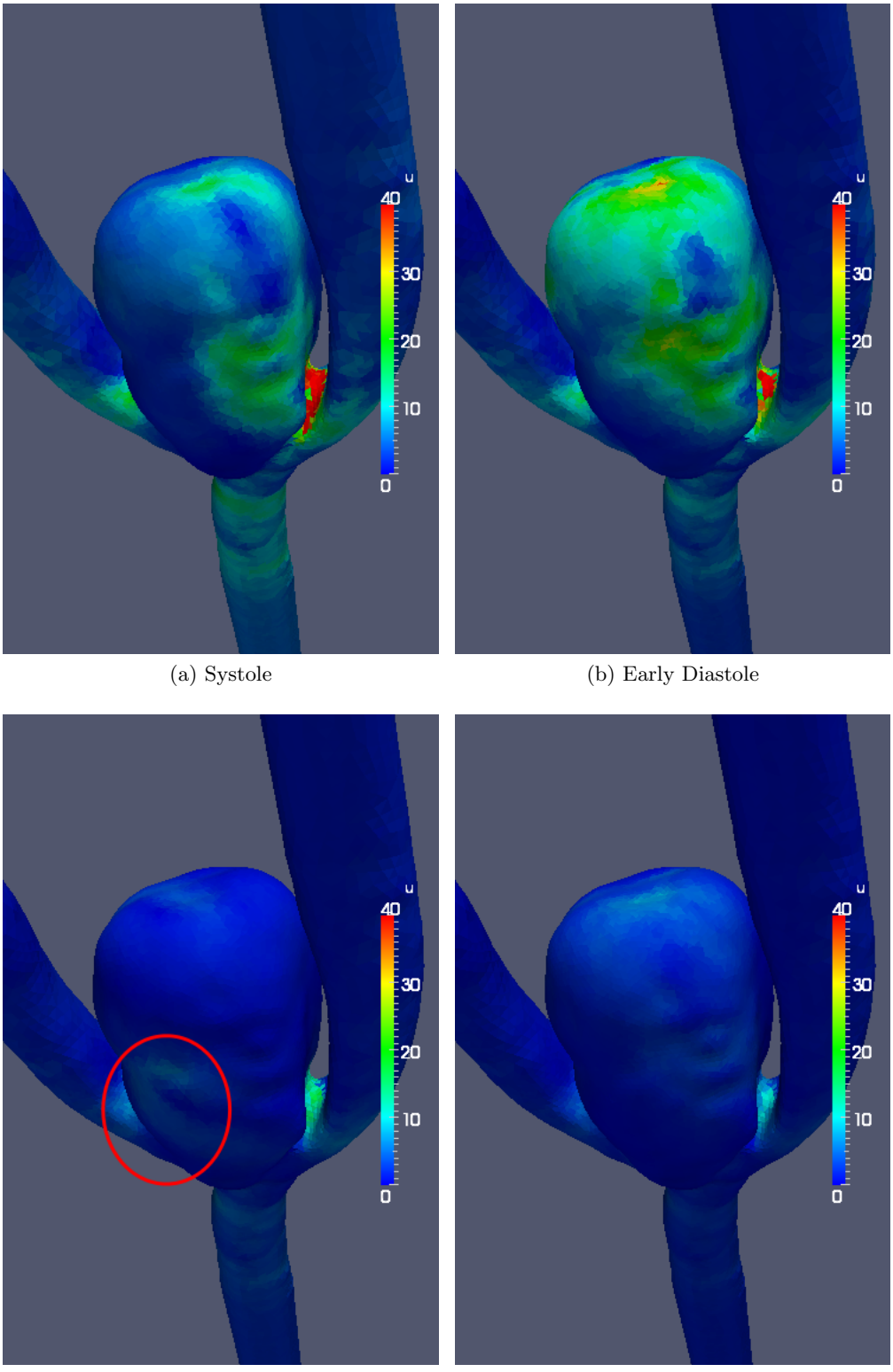

(a) Systole

(b) Early Diastole

(c) Middle Diastole

(d) End Diastole

Figure 7.7: The WSS for different parts of the high heart rate cardiac cycle.

7.3 Proper Orthogonal Decomposition

As part of the post-processing a POD of the velocity field stored after the simulation was done. We did two different decompositions, one normal decomposition and one where the aneurysm was isolated and the flow restricted to this part of the geometry. They will be referred to as the *normal decomposition* and *aneurysm decomposition* respectively.

The basis

In Figure 7.8 - 7.10 we visualized the basis functions for low and high heart rate and for the normal and aneurysm decomposition.

We see that the first basis is fairly similar in both high and low heart rate. The high basis is pushed a bit closer to the wall. This is evident from the inner product between the two which is 0.99 for the normal decomposition and 0.97 for the aneurysm decomposition

The second basis is much more spread out for the high heart rate compared to the low heart rate. The low basis has one certain area it wants to correct while the high basis tries to correct more sections at the same time. These observations is apparent for the third basis as well.

Looking at the normal basis we observe that the first basis contains most of the in- and out-going flow. The second and third basis is mostly distributed inside the aneurysm. Because of this and the fact that we are mostly interested in the flow inside the aneurysm, we will use the aneurysm decomposition for the remainder of this chapter.

We made an animation of the cardiac cycles where the basis was plotted separately over time

$$a_i^n \theta_i \text{ for i=1,2,3.} \tag{7.1}$$

The modes go from left to right such that mode 1 is on the left side and mode 3 is on the right side.

The animation can be found at http://folk.uio.no/haakonoo/master/animation/.

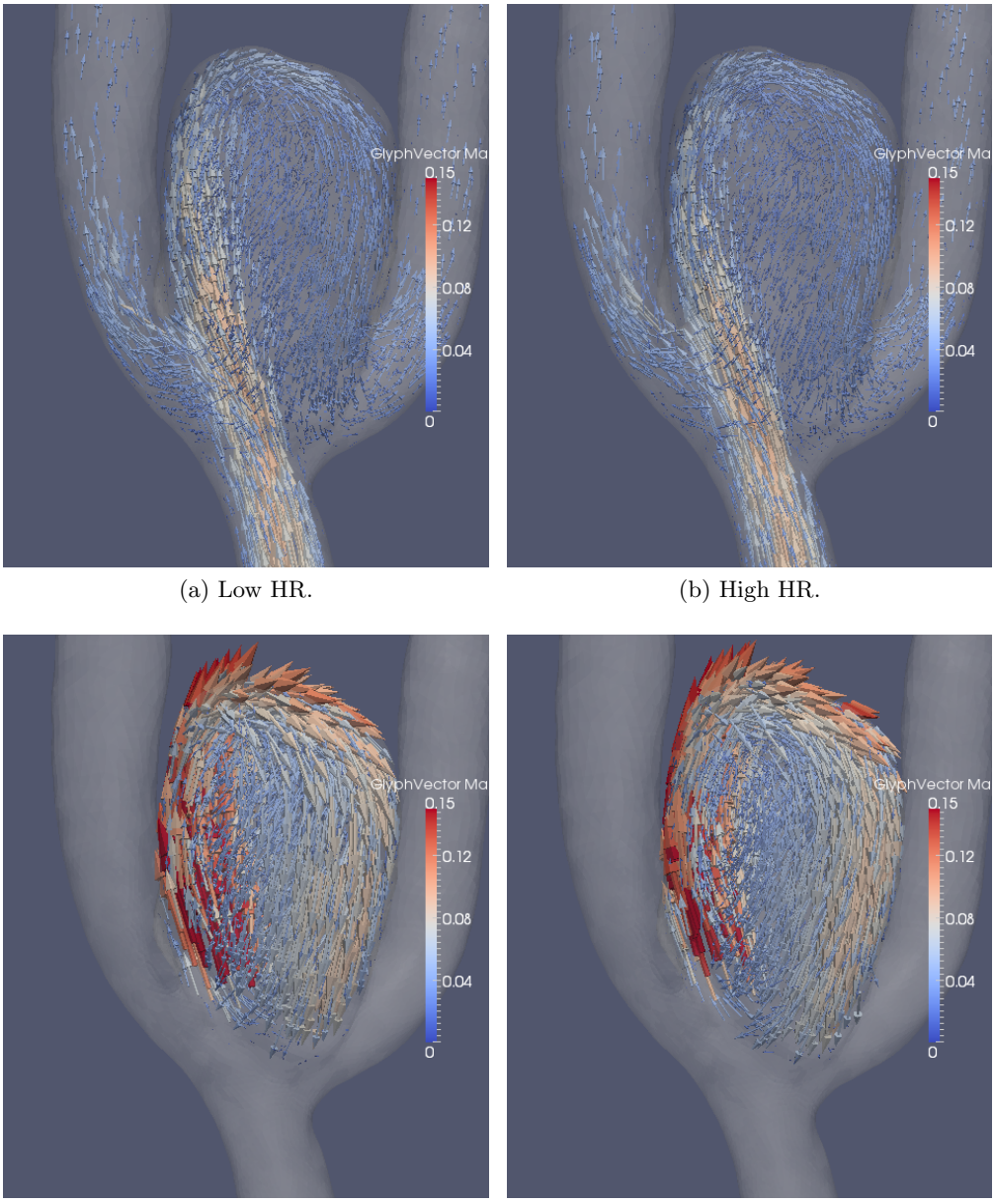

(a) Low HR.

(b) High HR.

(c) Low HR aneurysm.

(d) High HR aneurysm.

Figure 7.8: Basis 1 for low and high heart rate. Normal decomposition is a-d and aneurysm decomposition is c-d. The inner product between a-b is 0.99 and between c-d is 0.97.

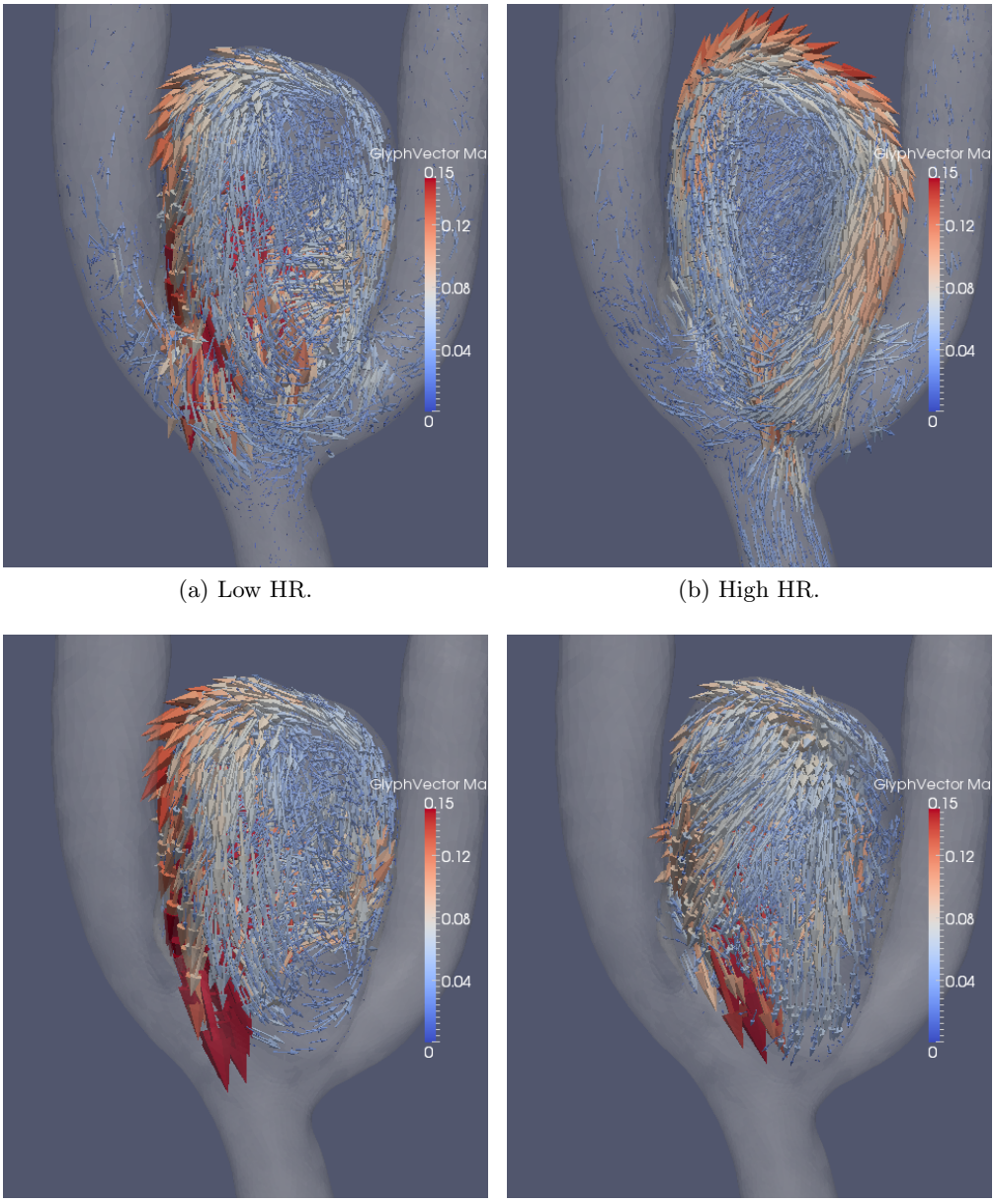

(a) Low HR.

(b) High HR.

(c) Low HR aneurysm.

(d) High HR aneurysm.

Figure 7.9: Basis 2 for low and high heart rate. Normal decomposition is a-d and aneurysm decomposition is c-d. The inner product between a-b is -0.55 and between c-d is 0.59.

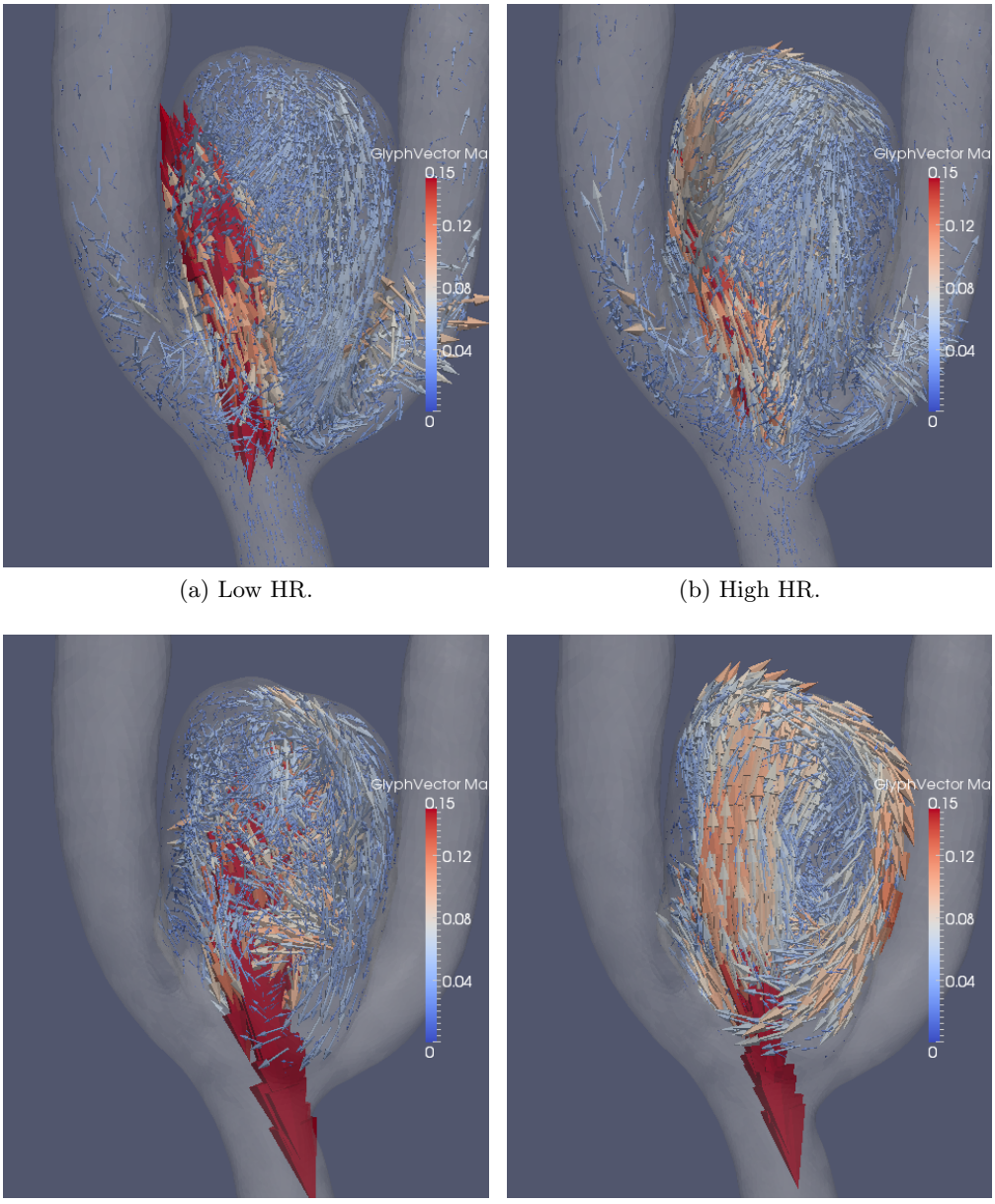

(a) Low HR.

(b) High HR.

(c) Low HR aneurysm.

(d) High HR aneurysm.

Figure 7.10: Basis 3 for low and high heart rate. Normal decomposition is a-d and aneurysm decomposition is c-d. The inner product between a-b is 0.75 and between c-d is 0.44.

Complexity of flow

We want to distinguish between complex and non-complex flow to explore whether there is a difference between high and low heart rate. Our hypothesis is that if more modes are needed to get a good representation of the velocity field, the flow can be considered to be more complex.

The square norm of the different modes divided by the square norm of the velocity was plotted

$$g_i(n) = \frac{\|a_i^n \theta_i\|_E^2}{\|u^n\|_E^2} \text{ for modes } i = 1, 2, ..., k. \tag{7.2}$$

In L^2 (because orthogonality), g_i has the nice property that all they sum up to one

$$\sum_{i=1}^{r} g_i(n) = \sum_{i=1}^{r} \frac{\|a_i^n \theta_i\|_{L^2(\Omega)}^2}{\|u^n\|_{L^2(\Omega)}^2} = \frac{\|\sum_{i=1}^{r} a_i^n \theta_i\|_{L^2(\Omega)}^2}{\|u^n\|_{L^2(\Omega)}^2} = \frac{\|u^n\|_{L^2(\Omega)}^2}{\|u^n\|_{L^2(\Omega)}^2} = 1. \tag{7.3}$$

In the plots we will also be able to see where in the cardiac cycle we get a more complex flow.

To test the hypothesis we plotted g_i for the flow in a cylinder with the same inflow condition as the aneurysm. The flow in a cylinder is a Poiseuille flow (the same as derived in Section 3.2) and can be considered to be non-complex. As a result of that we should expect the first mode to dominate completely. This we find to be true (see Figure 7.11), hence it justifies the hypothesis which was stated.

The norm we choose may affect the outcome of the result. We want to find the norm that best represents the velocity field. The H^1 norm contains the gradient of the velocity field and may give us information that the L^2 norm do not. This is because the rotation is captured in the gradient. The basis computed in the POD is optimal in L^2 and displays the kinetic energy, so L^2 should not be discarded. The orthogonality in L^2 is also a useful property.

We can see from Figure 7.12 that the differences in H^1 and L^2 are substantial for the first mode, especially for high heart rate. However, the other modes are fairly similar in shape and placement. It is also clear that the deviations that exists become greater in the H^1 norm. This is not surprising since the POD finds the best basis for the L^2 norm. We also find that the first drop in the H^1 norm is after the systole where the WSS was highest. This means that the H^1 norm should be considered.

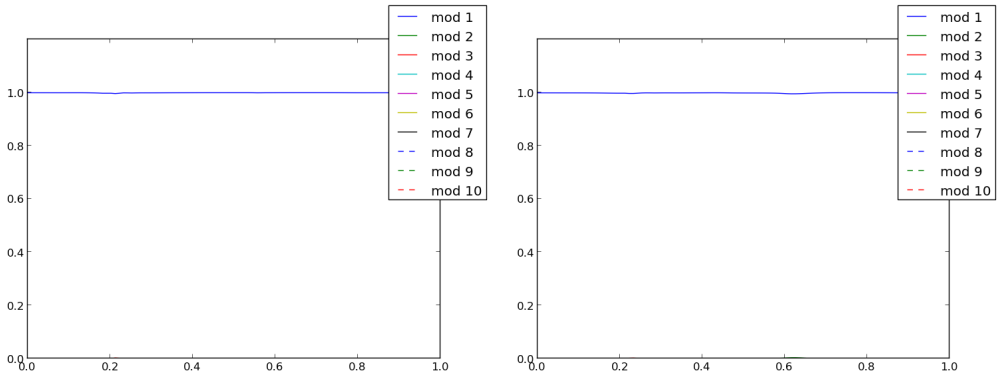

(a) Low HR L^2 norm (b) High HR L^2 norm

Figure 7.11: POD mode plot for high and low HR on a cylinder. We see that the first mode dominates the other modes.

We see a big difference in the complexity between high and low heart rate. For low heart rate we see that the first mode is fluctuating and does not have a massive drop. The high heart rate however has a big drop at the middle diastole and several modes are required to get a good approximation in the middle diastole time period. This is the same observation we made from the velocity and WSS pattern. These observations give reason to conclude that the flow with high heart rate is more complex than the low heart rate flow.

Another measure that can be used to state the complexity of the flow is the error of the span of k basis functions

$$f(k) = \frac{\sum_{n=1}^{M} \|u^n - \sum_{i=1}^{k} a_i^n \theta_i\|_E^2}{\sum_{n=1}^{M} \|u^n\|_E^2}. \tag{7.4}$$

We plotted this quantity for increasing values of k, see Figure 7.13. The L^2 norm gives a decreasing graph in such a way that the decrease in f becomes less and less as k increases, making the graph of f convex. It comes to a point where f decreases with almost the same amount for every k. Firstly this is expected as the POD basis is the best basis for u^n. Secondly it gives reason to conclude that after the first few basis functions are used, the remaining basis functions are equally important for portraying the flow. We also see that the first basis is by far the most important. We can see that the graph for both high and low heart rate has the same shape and that the difference in f between high and low heart rate are small as k increases.

We see that the H^1 norm is much higher than the L^2 norm. In H^1 we see that the graph for high heart rate in Figure 7.13b is not convex hence H^1 does not

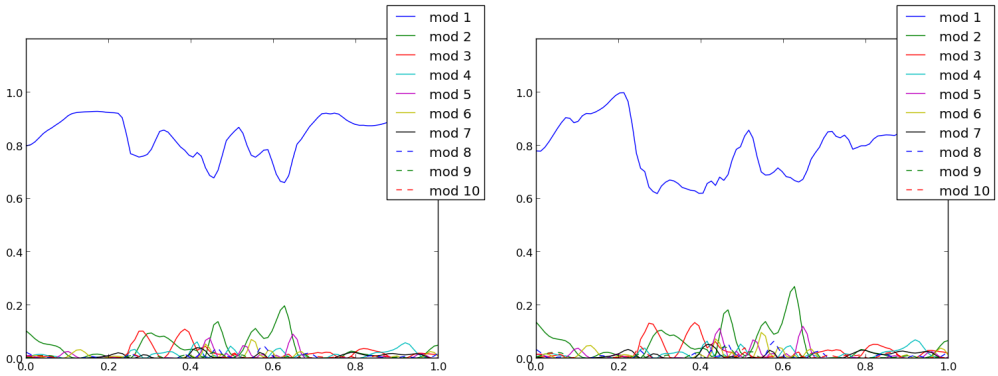

(a) Low HR L^2 norm

(b) Low HR H^1 norm

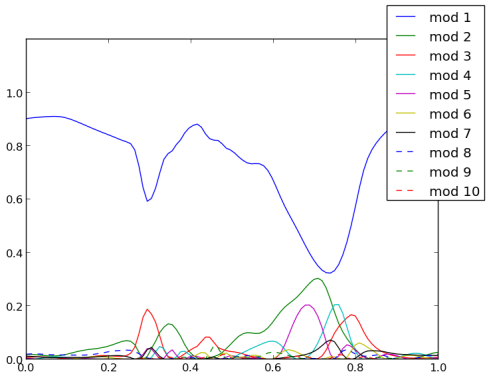

(c) High HR L^2 norm

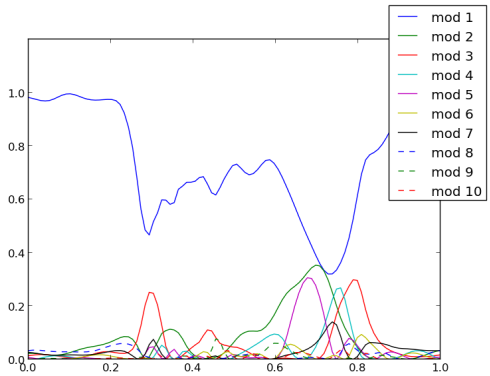

(d) High HR H^1 norm

Figure 7.12: Comparison of high and low HR with different norms. Rows represent heart rate and columns represent different norms. We see a difference in high and low heart rate. The H^1 norm displays different qualities than the L^2 norm.

share this property with L^2.

7.4 Findings

High heart rate may change the pattern of the blood flow in an aneurysm. The observations shows that the maximum WSS is larger due to heart rate increase and heart rate changes how the WSS is distributed. We have seen that the POD basis for high and low heart rate differ and that the best way of using POD is to isolate the aneurysm from the rest of the geometry and use the flow in the aneurysm to find the decomposition.

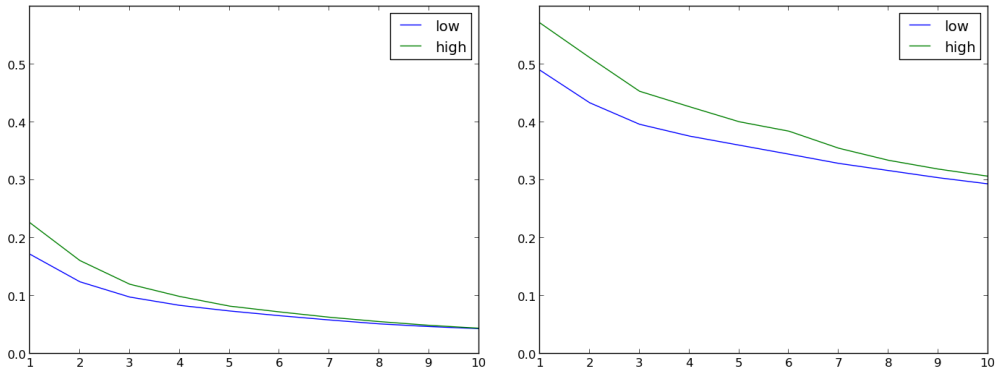

(a) L^2 norm (b) H^1 norm

Figure 7.13: Comparison of the error in POD approximation for high and low HR with different norms.

We have observed that H^1 captures the WSS changes that may not be found in L^2. POD analysis showed that the high heart rate was more complex and needed more basis functions to approximate the solution well. However, after the first few basis functions were used, the error in the basis approximations were essentially the same for high and low heart rate and the error decreased by the same amount when we used more basis functions. We found that the first basis function is by far the most important in the POD. The other functions of the POD can be thought of as corrections of the first mode in some parts of the cardiac cycle.

The observations made here encouraged us to continue the study with more aneurysms and to attempt to find a correlation between changes in flow and rupture.

Chapter 8

Quantitative results

In this chapter we have used twelve different aneurysms, both sidewall and bifurcation, where seven are known to have ruptured at a later time. We have marked the aneurysms from A1 to A12. The properties of the different aneurysms are given in Table 8.1. All the aneurysms are found in the MCA and are part of the database at the Simula research laboratory.

The aneurysms were segmented from CT angiograms using the Vascular Modelling ToolKit. Isolated aneurysm meshes as well as meshes with inflow and outflow arteries were available in the database. We did two simulations per aneurysm, one for low and one for high heart rate, both with the Newtonian fluid assumption. The mesh is chosen with number of cells from 700000 to 1900000. We used 8000 time steps in both low and high heart rate cases and 100 velocity fields were saved evenly distributed over the course of the last cycle.

For the post-processing of the aneurysms we calculated the average angle difference of the WSS between high and low heart rate

$$\phi(x) = \cos^{-1}\left(\frac{\overline{S_t^h}(x) \cdot \overline{S_t^l}(x)}{|\overline{S_t^h}(x)||\overline{S_t^l}(x)|}\right) \text{ for } x \in \partial\Omega. \tag{8.1}$$

We also calculated the average WSS magnitude ratio between high and low heart rate

$$\tau_r(x) = \frac{|\overline{S_t^h}(x)|}{|\overline{S_t^l}(x)|} \text{ for } x \in \partial\Omega. \tag{8.2}$$

As discussed in Section 3.2 it is a difference in the average inflow flux ratio. If no changes are present and the WSS is linearly dependent on the inflow flux

Aneurysm	Status	Geometry type
A1	Unruptured	Sidewall
A2	Unruptured	Bifurcation
A3	Ruptured	Bifurcation
A4	Unruptured	Sidewall
A5	Unruptured	Sidewall
A6	Ruptured	Bifurcation
A7	Ruptured	Bifurcation
A8	Ruptured	Bifurcation
A9	Ruptured	Sidewall
A10	Ruptured	Bifurcation
A11	Ruptured	Bifurcation
A12	Unruptured	Bifurcation

Table 8.1: Properties of aneurysms studied.

we should expect the value of τ_r to be constant and to be equal to the inflow flux ratio 0.87.

The POD was computed on the isolated aneurysms. The inner product was computed between the different basis for high and low heart rate (see Table 8.3) and the functions f and g (defined in Section 7.3) were computed for both L^2 and H^1.

We plotted ϕ and τ_r and as a reference we plotted $|\overline{S_t^l}|$. Together with these quantities we plotted f and g for both L^2 and H^1. These plots can be viewed in Figures 8.2 - 8.13.

To compare the changes we found in the heart rates we did simulations with the non-Newtonian viscosity model modified Cross (see Section 3.5) and used the low heart rate as inflow.

8.1 Changes between high and low heart rate

By the Figures 8.2 - 8.13 we can see that there are changes in the WSS between the two heart rates. For the angle we see changes up to 30 °. There are regions where the WSS magnitude for the high heart rate are twise of that for the low heart rate case and regions where the opposite is true

$$\tau_r(x) \geq 2 \text{ for some } x \qquad \tau_r(y) \leq 0.5 \text{ for some } y. \tag{8.3}$$

We see as predicted that the WSS ratio 0.87 is in the parent and outflow arteries, hence it will be most useful to look at the changes that differ from this value. It is also worth noticing that even though cases A3, A4 and A9 give high values in the angle and ratio plots, we can see from the reference plot that the WSS very low in these regions.

Aneurysm	Angle	Magnitude
A1	0.010	0.111
A2	0.025	0.079
A3	0.014	0.090
A4	0.000	0.007
A5	0.001	0.074
A6	0.023	0.041
A7	0.019	0.134
A8	0.172	0.406
A9	0.004	0.187
A10	0.032	0.068
A11	0.001	0.003
A12	0.002	0.194

Table 8.2: Portion of noticeable changes in angle and magnitude of the WSS between high and low heart rate.

To get a better measure of the changes we calculated the portion of the area with noticeable angle and magnitude changes. We defined this as

$$\frac{Area(\Gamma_\phi)}{Area(\Omega_{WSS})} \text{ for } \Gamma_\phi = \{x \in \Omega_{WSS} : \phi(x) \geq 20\,^\circ\} \tag{8.4}$$

$$\frac{Area(\Gamma_\tau)}{Area(\Omega_{WSS})} \text{ for } \Gamma_\tau = \{x \in \Omega_{WSS} : \tau_r(x) \leq \frac{0.87}{1.3} \text{ or } \tau_r(x) \geq 0.87 \cdot 1.3\} \quad (8.5)$$

where $\Omega_{WSS} = \{x \in \partial\Omega_A : \overline{S_t^l}(x) \geq 1Pa\}$ and Ω_A denotes the isolated aneurysm. The measure 8.4 signifies the portion of the aneurysm that have WSS angle differences greater than 20 °. The measure 8.5 signifies the portion of the aneurysm that have WSS magnitude differences greater than 30% with respect to the influx ratio 0.87. The calculated values can be viewed in Table 8.2. The A8 aneurysm sticks out with considerably higher values on the angle and magnitude than any of the other aneurysms. The mean value is 0.0256 for the angle and 0.116 for the magnitude.

We can see by the plots g and f for both L^2 and H^1 that the error in the POD approximation is larger in the high heart rate case. As a measure of complexity we use $f(1)$. We calculated that the measure range from $0.02 - 0.07$ for low heart rate and $0.08 - 0.24$ for high heart rate in L^2. The ratio $f^h(1)/f^l(1)$ is greater than 1.8 for all cases by using L^2 and for nine out of the twelve cases this ratio is greater than 3. With the H^1 norm the measure range from $0.15 - 0.25$ for low heart rate and $0.27 - 0.56$ for high heart rate. The ratio here varies from $1.6 - 2.3$. These observations lead us to conclude that the high heart rate flow is more complex than the low heart rate flow.

It is high agreement in the inner product between the first POD basis functions (see Table 8.3). Again A8 stands out as the most different. For the other modes we see that A6 is most different. We investigated A6 and found that $\left(\phi_2^l, \phi_3^h\right)_\Omega = 0.802$ and $\left(\phi_3^l, \phi_2^h\right)_\Omega = -0.763$. Also when we look at the mode plots and the POD error (Figure 8.7) we see that basis two and three have very little impact on the over all solution. Basis three in A2 have low agreement, but again by the mode plots (Figure 8.3 red line) we see that mode three have very little impact. Other aneurysms with differences in the inner product basis two and three are A3, A7 and A8.

8.2 Rupture

We want to investigate if there is a correlation between rupture and changes in flow or WSS.

We use the computed values in Table 8.2 to group the aneurysms with changes in average WSS angle and magnitude. For the differences in WSS angle we can use values that are greater than 0.01 to differentiate into groups. Cases with this property is A1-A3, A6-A8 and A10, hence two out of five unruptured aneurysms and four out of seven ruptured. For the differences in WSS

Aneurysm	Mode 1	Mode 2	Mode 3
A1	0.989	−0.917	0.819
A2	0.994	0.929	−0.466
A3	0.995	−0.867	0.616
A4	0.990	0.930	0.922
A5	0.991	0.974	0.941
A6	0.998	0.205	0.218
A7	0.991	0.759	0.770
A8	0.942	0.695	−0.511
A9	0.991	0.928	−0.886
A10	0.991	−0.931	0.845
A11	0.994	0.854	0.854
A12	0.989	−0.944	0.957

Table 8.3: Inner product between modes of high and low heart rate.

magnitude we can use values that are greater than 0.1. Then we get cases A1, A7-A9 and A12, hence two of five unruptuerd and three of seven ruptured aneurysms. Based on these results one can not make a claim that more changes in flow or WSS as a result of heart rate implies higher rupture risk.

For the complexity there is no clear value for $f(1)$ where we can distinguish the aneurysms into groups with high complexity vs groups with low complexity.

8.3 Changes from heart rate compared to changes in non-Newtonian blood modeling

To set the changes between high and low heart rate in perspective we will compare them to the changes in Newtonian and non-Newtonian modeling of blood.

To compare the two we will use Pearson correlation

$$r_{xy} = \frac{\sum_{i=1}^{n}(x_i - \overline{x})(y_i - \overline{y})}{\sigma_x \sigma_y} \tag{8.6}$$

were σ is the standard deviation. It is a measure of how correlated a quantity is and $|r_{xy}| = 1$ means there is a linear relationship between x and y. Any other value of r_{xy} indicate the degree of linear dependence between x and y (zero being no linear dependence at all).

We used the average WSS magnitude over the aneurysm to compute the correlation, that is we calculate r_{xy} by letting

$$x_i = |\overline{S_t^a}(z_i)| \qquad y_i = |\overline{S_t^b}(z_i)| \text{ for } z_i \in \partial\Omega_A \tag{8.7}$$

were a, b denotes either low and high heart rate or Newtonian and non-Newtonian modeling of blood. Calculations can be viewed in Table 8.4. We also plotted the average WSS magnitude vector for the three different simulations high heart rate Newtonian fluid, low heart rate Newtonian fluid and low heart rate non-Newtonian fluid (see Figure 8.1). By Table 8.4 we see that there are strong correlations for both heart rate and viscosity. The mean correlation is lower in the heart rate case (0.991 to 0.986) due to the lower correlation in A1 and A8. In seven of the aneurysms the viscosity correlation is lower than the heart rate, in two of the cases the correlation was equal and the remaining three the correlation were higher for heart rate. However, the differences are not substantial.

We calculated the measures 8.4 and 8.5 (where the influx ratio is 1) for Newtonian and non-Newtonian flow as well. These can be found in Table 8.5. The changes in WSS magnitude were fairy the same as in the heart rate case. The mean value was 0.096 compared to 0.116 as we found in Section 8.1 and the highest value was 0.440 compared to 0.406. The WSS angle changes were also fairly similar, with the exception of the A8 aneurysm. The mean value in Newtonian case is 0.008 where as it was 0.025 in the heart rate case and the maximum is 0.027 compared to 0.172 in the heart rate case.

Based on these observations we conclude that the changes in the WSS magnitude from heart rate are in the same order as the changes we get from using a varying viscosity model. The direction of the WSS may prone to more changes when heart rate is increased compared to if one uses a non-Newtonian model.

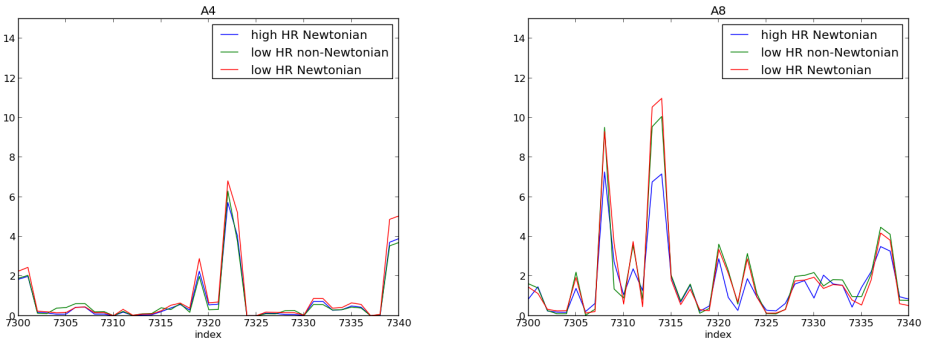

(a) A4 (b) A8

Figure 8.1: Average WSS magnitude vector plotted for low heart rate non-Newtonian flow, high heart rate Newtonian flow and low heart rate Newtonian flow. A4 showed highest correlation while A8 showed lowest correlation.

Aneurysm	Heart rate	Newtonian
A1	0.953	0.989
A2	0.995	0.995
A3	0.996	0.993
A4	0.999	0.989
A5	0.996	0.996
A6	0.994	0.986
A7	0.985	0.995
A8	0.940	0.989
A9	0.998	0.995
A10	0.987	0.985
A11	0.995	0.989
A12	0.994	0.993

Table 8.4: Pearson correlation number r for the average WSS. Column 2 is for the correlation between high and low heart rate. Column 3 is for the correlation between Newtonian and non-Newtonian blood modeling.

Aneurysm	Angle	Magnitude
A1	0.001	0.022
A2	0.012	0.047
A3	0.027	0.127
A4	0.000	0.440
A5	0.000	0.031
A6	0.018	0.109
A7	0.005	0.056
A8	0.007	0.061
A9	0.002	0.113
A10	0.012	0.075
A11	0.005	0.039
A12	0.003	0.032

Table 8.5: Portion of noticeable changes in angle and magnitude of the WSS between Newtonian and non-Newtonian blood modeling.

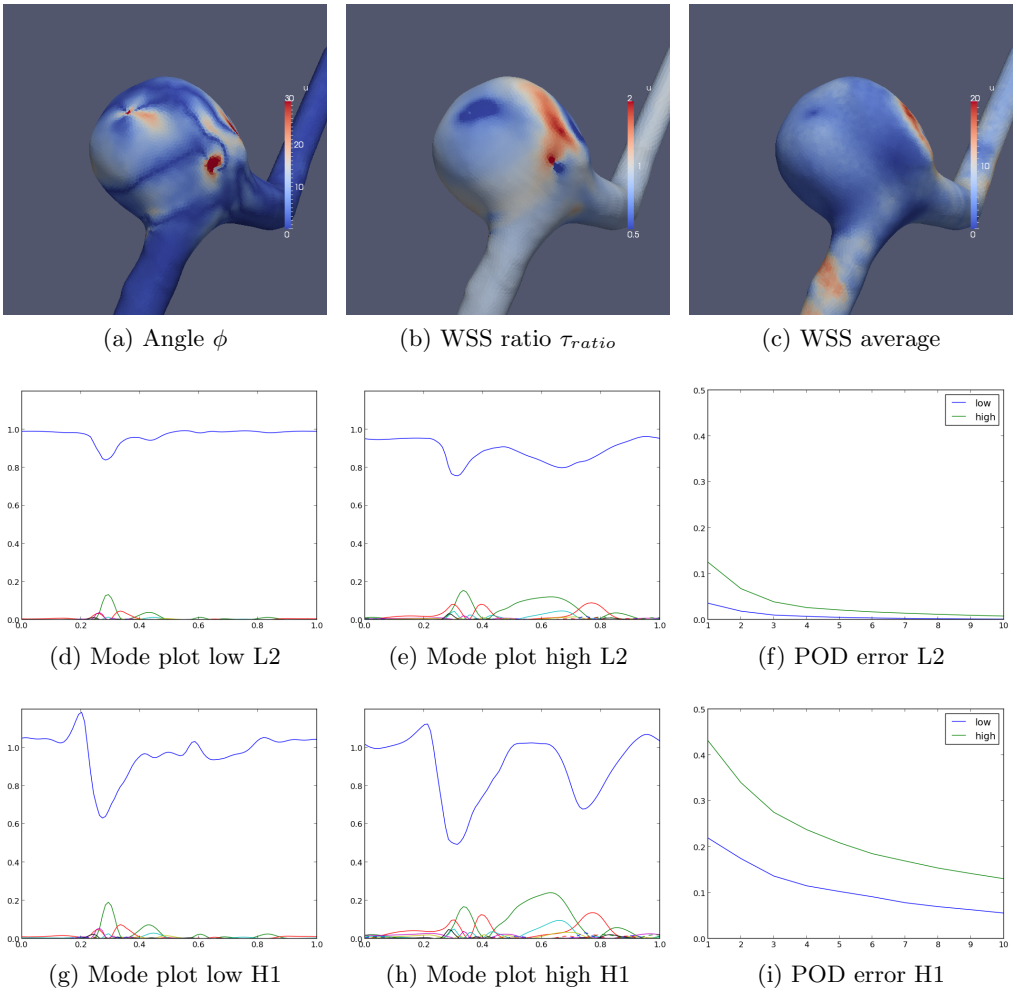

(a) Angle ϕ (b) WSS ratio τ_{ratio} (c) WSS average

(d) Mode plot low L2 (e) Mode plot high L2 (f) POD error L2

(g) Mode plot low H1 (h) Mode plot high H1 (i) POD error H1

Figure 8.2: A1.

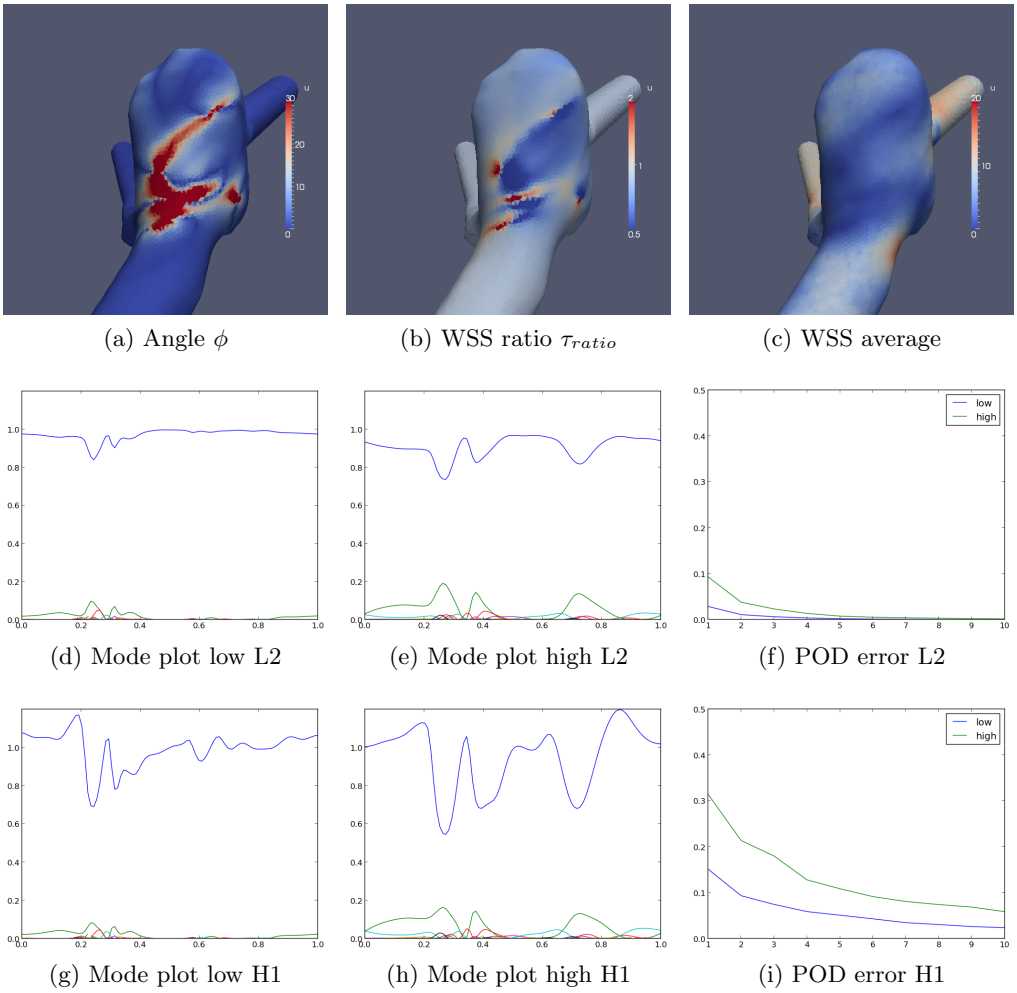

(a) Angle ϕ (b) WSS ratio τ_{ratio} (c) WSS average

(d) Mode plot low L2 (e) Mode plot high L2 (f) POD error L2

(g) Mode plot low H1 (h) Mode plot high H1 (i) POD error H1

Figure 8.3: A2.

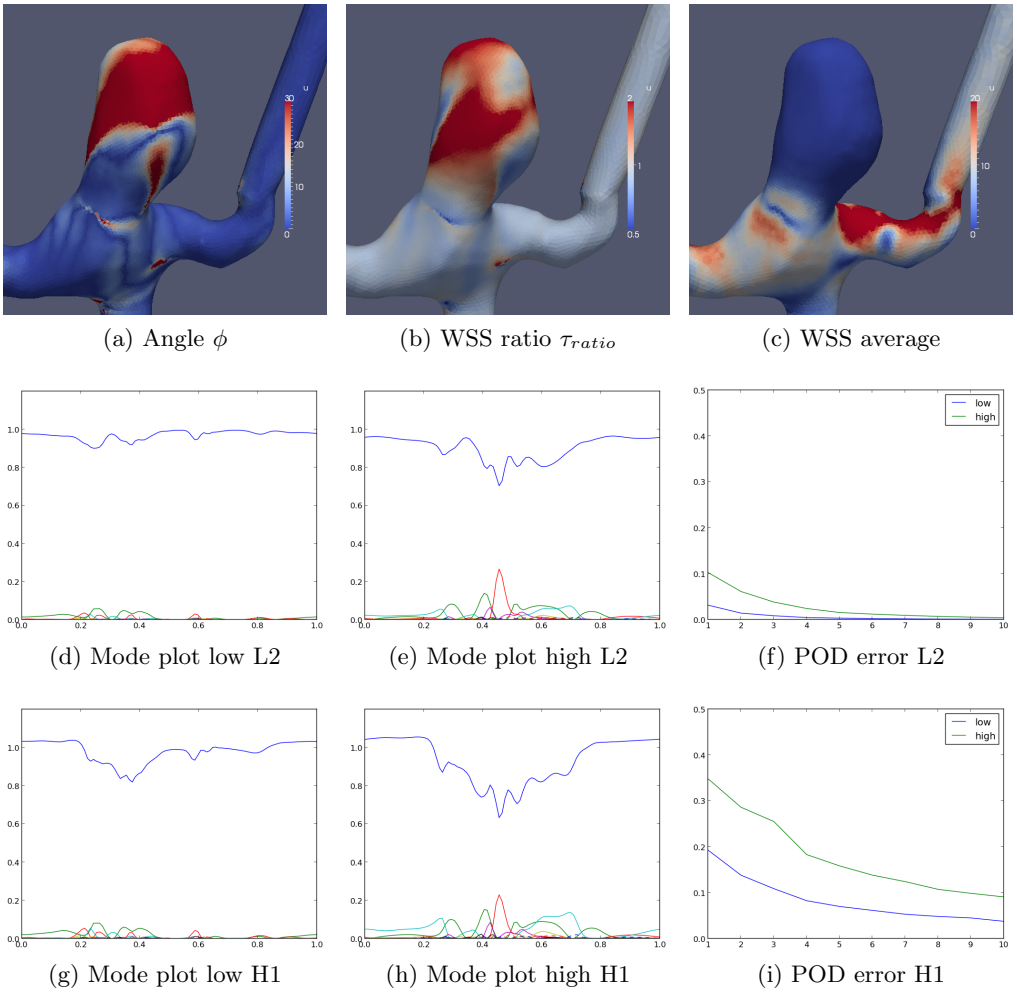

(a) Angle ϕ (b) WSS ratio τ_{ratio} (c) WSS average

(d) Mode plot low L2 (e) Mode plot high L2 (f) POD error L2

(g) Mode plot low H1 (h) Mode plot high H1 (i) POD error H1

Figure 8.4: A3.

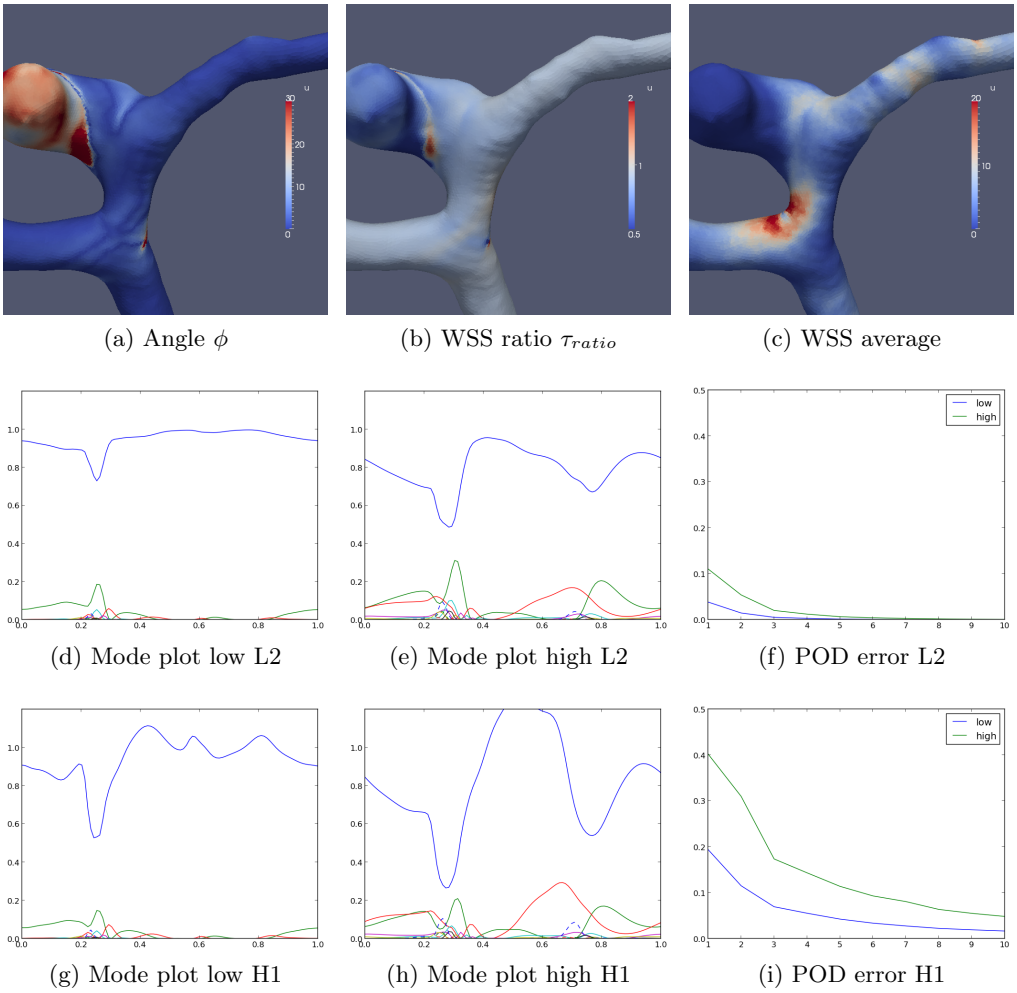

(a) Angle ϕ (b) WSS ratio τ_{ratio} (c) WSS average

(d) Mode plot low L2 (e) Mode plot high L2 (f) POD error L2

(g) Mode plot low H1 (h) Mode plot high H1 (i) POD error H1

Figure 8.5: A4.

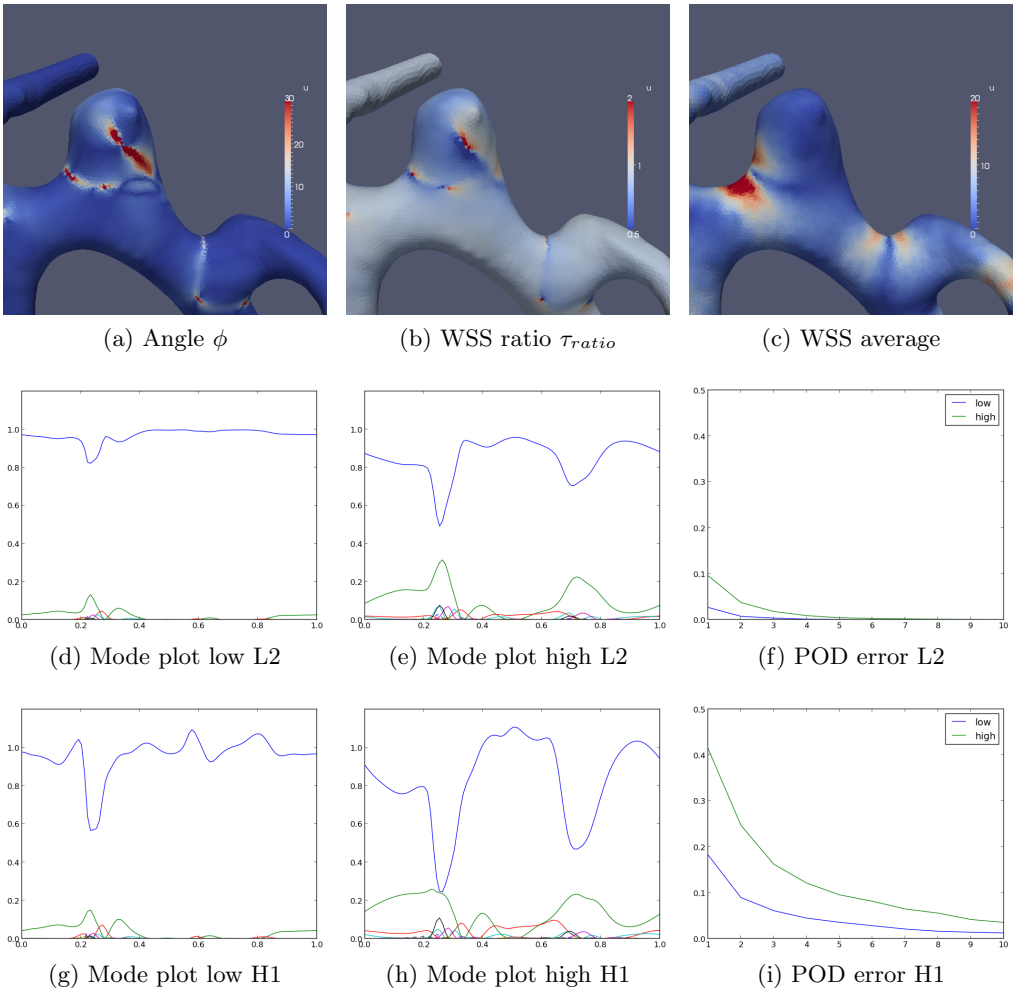

(a) Angle ϕ (b) WSS ratio τ_{ratio} (c) WSS average

(d) Mode plot low L2 (e) Mode plot high L2 (f) POD error L2

(g) Mode plot low H1 (h) Mode plot high H1 (i) POD error H1

Figure 8.6: A5.

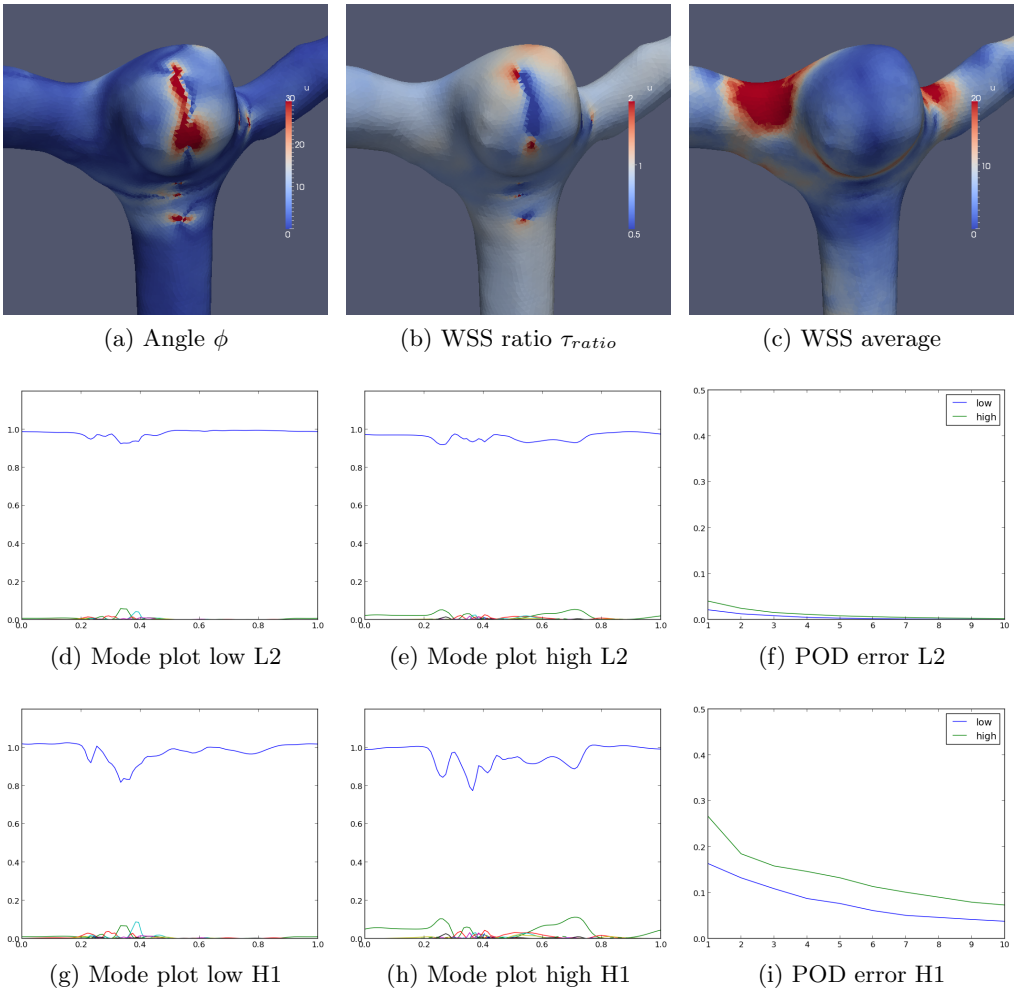

(a) Angle ϕ (b) WSS ratio τ_{ratio} (c) WSS average

(d) Mode plot low L2 (e) Mode plot high L2 (f) POD error L2

(g) Mode plot low H1 (h) Mode plot high H1 (i) POD error H1

Figure 8.7: A6.

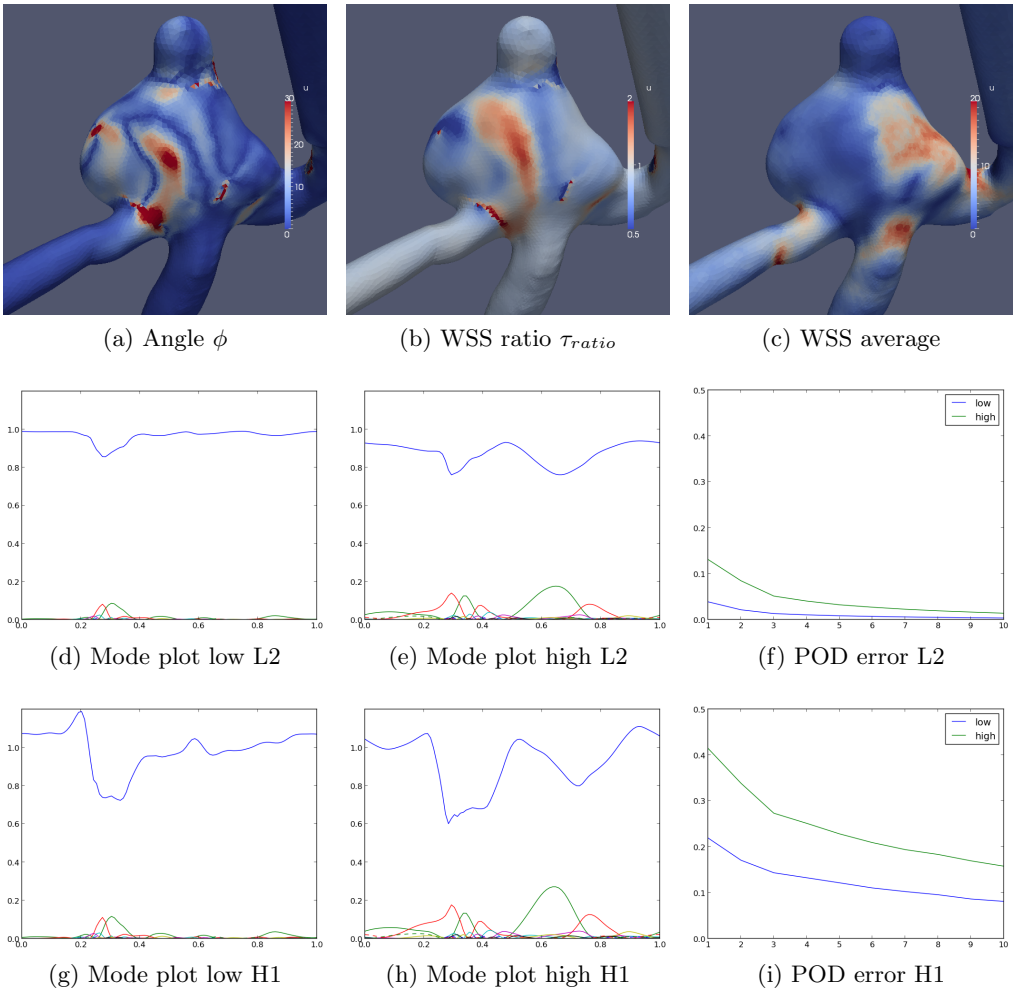

(a) Angle ϕ (b) WSS ratio τ_{ratio} (c) WSS average

(d) Mode plot low L2 (e) Mode plot high L2 (f) POD error L2

(g) Mode plot low H1 (h) Mode plot high H1 (i) POD error H1

Figure 8.8: A7.

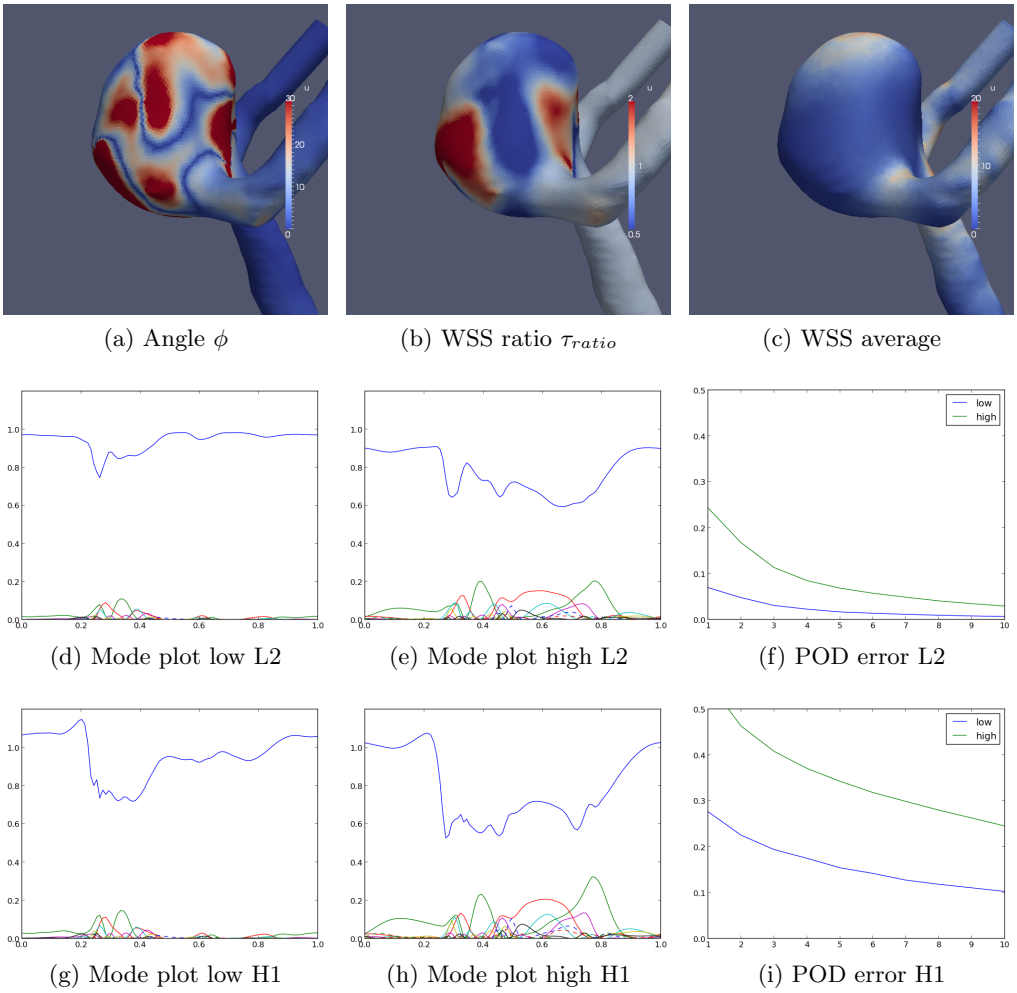

(a) Angle ϕ (b) WSS ratio τ_{ratio} (c) WSS average

(d) Mode plot low L2 (e) Mode plot high L2 (f) POD error L2

(g) Mode plot low H1 (h) Mode plot high H1 (i) POD error H1

Figure 8.9: A8.

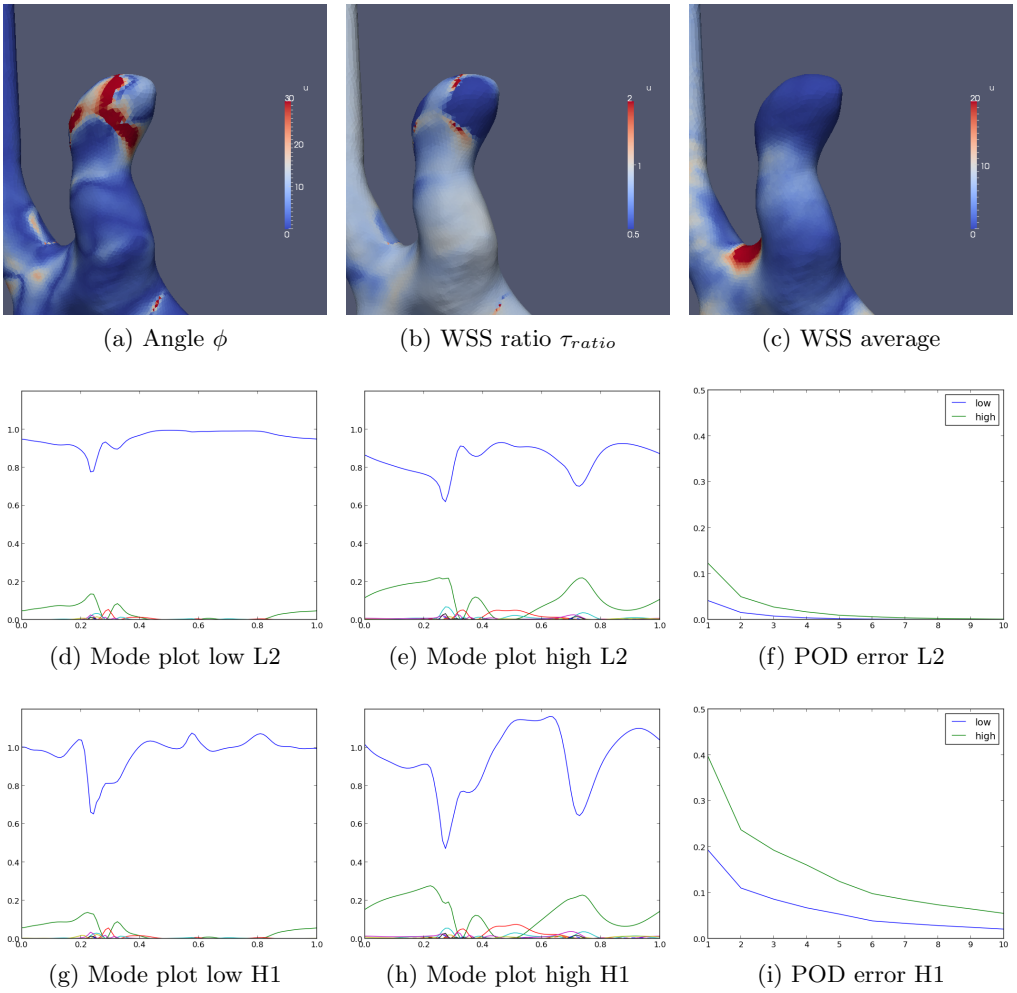

(a) Angle ϕ (b) WSS ratio τ_{ratio} (c) WSS average

(d) Mode plot low L2 (e) Mode plot high L2 (f) POD error L2

(g) Mode plot low H1 (h) Mode plot high H1 (i) POD error H1

Figure 8.10: A9.

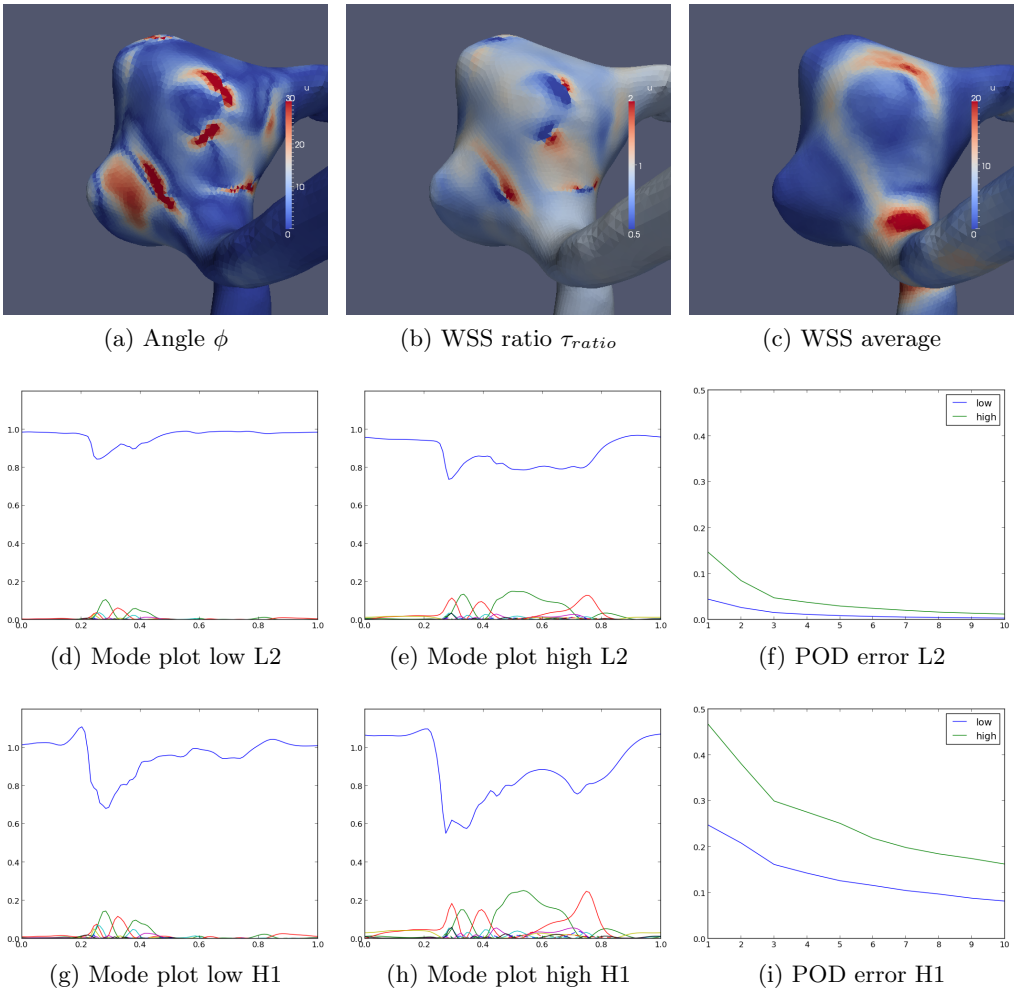

(a) Angle ϕ (b) WSS ratio τ_{ratio} (c) WSS average

(d) Mode plot low L2 (e) Mode plot high L2 (f) POD error L2

(g) Mode plot low H1 (h) Mode plot high H1 (i) POD error H1

Figure 8.11: A10.

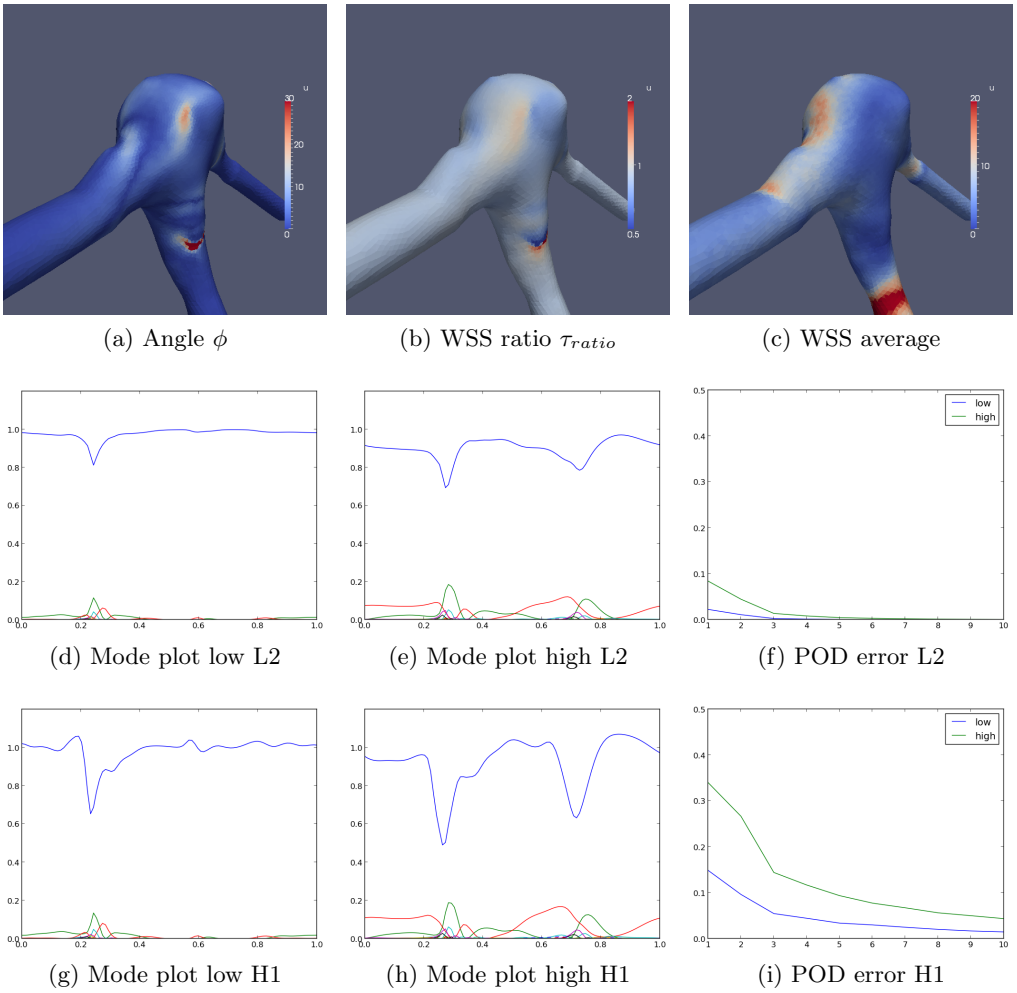

(a) Angle ϕ (b) WSS ratio τ_{ratio} (c) WSS average

(d) Mode plot low L2 (e) Mode plot high L2 (f) POD error L2

(g) Mode plot low H1 (h) Mode plot high H1 (i) POD error H1

Figure 8.12: A11.

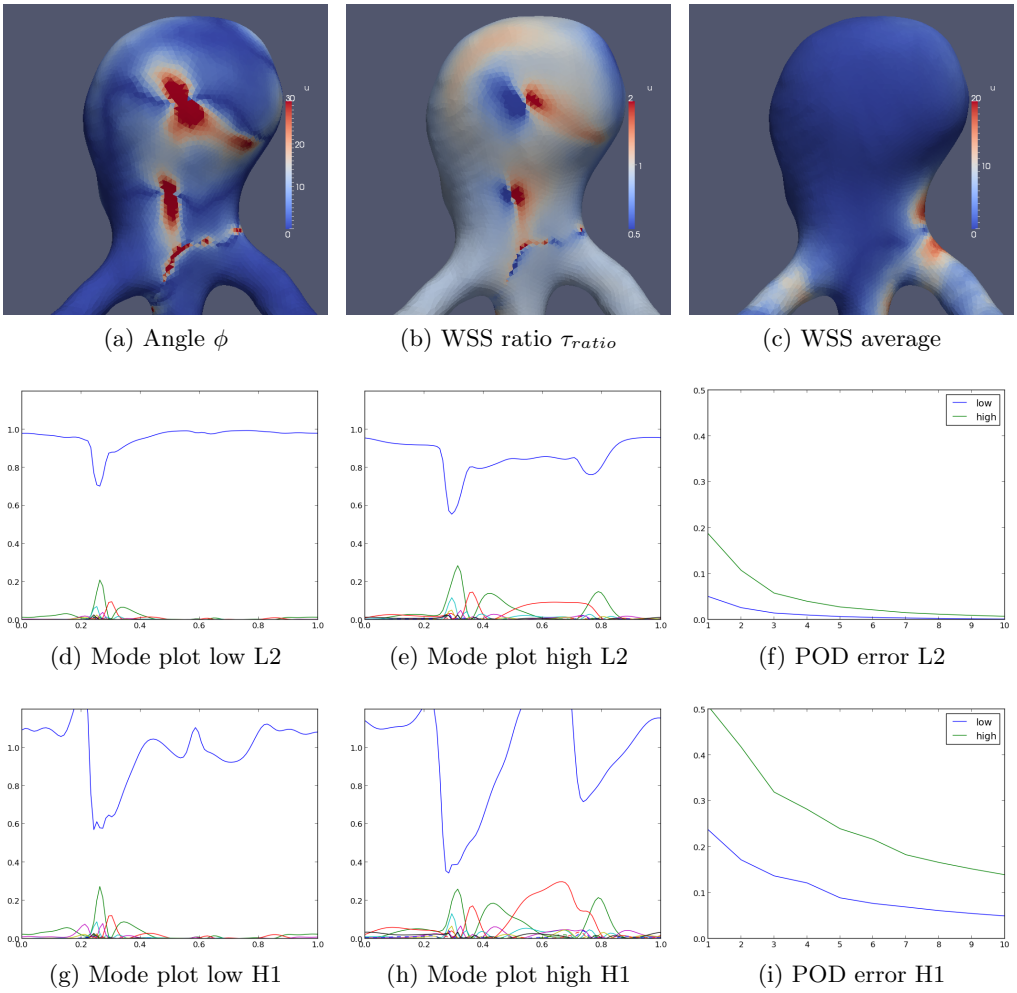

(a) Angle ϕ (b) WSS ratio τ_{ratio} (c) WSS average

(d) Mode plot low L2 (e) Mode plot high L2 (f) POD error L2

(g) Mode plot low H1 (h) Mode plot high H1 (i) POD error H1

Figure 8.13: A12.

Chapter 9

Discussion

We have demonstrated that the flow in aneurysms change for different heart rates. The severity of the changes were dependent on the geometry of the aneurysm, however we did not find any particular type of aneurysm more prone to these changes. We found that the POD error increased when we used high heart rate inflow. The error increased by a factor of three for almost all cases in L^2 and by a factor of $1.6-2.3$ in H^1. Four out of seven ruptured and two out of five unruptured aneurysms had noticeable WSS angle changes. Three out of seven ruptured and two out of five unruptured aneurysms had noticeable WSS magnitude changes. This is in the range of expected in a random selection and we can not claim a correlation with changes and rupture.

In perspective, changes in WSS magnitude were of the same order as the changes we find using a non-linear viscosity model. We found high correlation of the WSS in both with respect to the two viscosity models and the two heart rates. We found that in one case (A8) there were considerable differences in WSS direction in the heart rate case (angle difference greater than $20\,^\circ$ in 17% of the aneurysm). Changes of this magnitude were not found using non-Newtonian blood modeling.

9.1 Limitations of the study

In this study we used several assumptions and generalized the mathematical model. First we only used one set of inflow heart rates and they were not patient specific. To draw a firmer conclusion we would have to test for many sets of different inflow profiles and do a statistical analysis of the result. Also

the inflow heart rates came from Doppler images and where we took measures to be sure the profiles extracted matched the images, we can not be sure of the error in the image itself.

Secondly, the rigid wall assumption may be a cause of error. Elastic walls may help to dampen the impact of the blood flow on the aneurysm and prevent pattern changes to occur. This may again lead to less complex flow especially for the higher heart rate as the hemodynamic forces are prone to faster changes.

Thirdly, the laminar flow assumption may be a source of error and the reason we were not able to get a clear distinctions in the complexity. Valen-Sendstad et al. [25] did a study of flow on the same aneurysms used in this thesis without the use of the laminar assumption. They found that cases A3, A6-A8 and A10[1] had unstable flow with turbulent fluctuations.

Finally we have other assumptions in our model like traction free outflow boundary, Newtonian fluid and neglecting gravity all of which may have an effect on the solution and the results.

9.2 The importance of this study

CFD studies will always be subject to assumptions and different variables. When a study is to be performed one is faced with picking variables and assumptions in the study. Therefore it is important to quantify which assumptions and variables that makes most impact on the solution such that this knowledge can be used to perform better studies. This study is a part of this process regarding a variable which seldom gets noticed. We found that as long as the Newtonian assumption is used there will be no need to consider the heart rate as a variable. Øyvind Evju [28] analysed the non-Newtonian effects in intracranial aneurysms concluding that the effects are small compared to other variables. For our study this means that the effects of heart rate is relatively small as well and can be neglected.

9.3 Conclusion

We have shown that heart rate may change the pattern of the velocity field in aneurysms. The velocity field may become more complex due to an increase

[1]The aneurysms have been renumbered in this thesis.

in heart rate. The increase in complexity do not result in big differences in the average WSS. We found that the changes is of the same order as the changes from modeling blood as a non-Newtonian fluid. Seeing as other studies have concluded that the non-Newtonian effects is negligible we conclude that the heart rate is not important to consider in further studies.

Bibliography

[1] C. Anderson, C. N. Mhurchu, D. Scott, D. Bennett, K. Jamrozik, G. Hankey, et al. Triggers of subarachnoid hemorrhage role of physical exertion, smoking, and alcohol in the australasian cooperative research on subarachnoid hemorrhage study (across). *Stroke*, 34(7):1771–1776, 2003.

[2] G. Austin, S. Fisher, D. Dickson, D. Anderson, and S. Richardson. The significance of the extracellular matrix in intracranial aneurysms. *Annals of Clinical & Laboratory Science*, 23(2):97–105, 1993.

[3] L. Boussel, V. Rayz, C. McCulloch, A. Martin, G. Acevedo-Bolton, M. Lawton, R. Higashida, W. S. Smith, W. L. Young, and D. Saloner. Aneurysm growth occurs at region of low wall shear stress patient-specific correlation of hemodynamics and growth in a longitudinal study. *Stroke*, 39(11):2997–3002, 2008.

[4] J. L. Brisman, J. K. Song, and D. W. Newell. Cerebral aneurysms. *New England Journal of Medicine*, 355(9):928–939, 2006.

[5] J. R. Cebral and M. Raschi. Suggested connections between risk factors of intracranial aneurysms: A review. *Annals of biomedical engineering*, 2012.

[6] N. K. de Rooij, F. H. H. Linn, J. A. van der Plas, A. Algra, and G. J. E. Rinkel. Incidence of subarachnoid haemorrhage: a systematic review with emphasis on region, age, gender and time trends. *J Neurol Neurosurg Psychiatry*, 78:1365–1372, 2007.

[7] C. Dewey Jr, S. Bussolari, M. Gimbrone Jr, P. Davies, et al. The dynamic response of vascular endothelial cells to fluid shear stress. *Journal of biomechanical engineering*, 103(3):177, 1981.

[8] P. Holmes, J. L. Lumley, and G. Berkooz. *Turbulence, coherent structures, dynamical systems and symmetry.* Cambridge University Press, 1998.

[9] D. L. Hoyert, E. Arias, B. L. Smith, S. L. Murphy, and K. D. Kochanek. National vital statistics reports. *Deaths: Final Data for 1999*, 49, 2012.

[10] J. D. Humphrey. *Cardiovascular solid mechanics: cells, tissues, and organs*. Springer Verlag, 2002.

[11] J. Jiang, C. Strother, et al. Computational fluid dynamics simulations of intracranial aneurysms at varying heart rates: a" patient-specific" study. *Journal of biomechanical engineering*, 131(9):091001, 2009.

[12] L.-D. Jou, G. Wong, B. Dispensa, M. T. Lawton, R. T. Higashida, W. L. Young, and D. Saloner. Correlation between lumenal geometry changes and hemodynamics in fusiform intracranial aneurysms. *American journal of neuroradiology*, 26(9):2357–2363, 2005.

[13] V. Kumar, N. Abbas, Fausto, and R. Mitchell. *Robbins basic pathology*. Saunders, 2007.

[14] P. K. Kundu, I. M. Cohen, and D. R. Downing. *Fluid Mechanics*. Elsevier, fifth edition, 2012.

[15] M. Levesque, R. Nerem, et al. The elongation and orientation of cultured endothelial cells in response to shear stress. *Journal of biomechanical engineering*, 107(4):341, 1985.

[16] D. Luchtenburg, B. Noack, and M. Schlegel. An introduction to the pod galerkin method for fluid flows with analytical examples and matlab source codes. Technical report, Technical Report 01/2009, Berlin Institute of Technology, Berlin, Germany, 2009.

[17] A. Mantha, C. Karmonik, G. Benndorf, C. Strother, and R. Metcalfe. Hemodynamics in a cerebral artery before and after the formation of an aneurysm. *American Journal of Neuroradiology*, 27(5):1113–1118, 2006.

[18] K.-A. Mardal, A. Logg, and G. N. Wells. *Automated Solution of Differntial Equations by the Finite Element Method*. Springer, 2011.

[19] M. Matsuda, K. Watanabe, A. Saito, K.-i. Matsumura, and M. Ichikawa. Circumstances, activities, and events precipitating aneurysmal subarachnoid hemorrhage. *Journal of Stroke and Cerebrovascular Diseases*, 16(1): 25–29, 2007.

[20] H. Meng, V. Tutino, J. Xiang, and A. Siddiqui. High wss or low wss? complex interactions of hemodynamics with intracranial aneurysm initiation, growth, and rupture: Toward a unifying hypothesis. *American Journal of Neuroradiology*, 2013.

[21] G. J. E. Rinkel, M. Djibuti, A. Algra, and J. van Gijn. Prevalence and risk of rupture of intracranial aneurysms: A systematic review. *Stroke*, 29:251–256, 1998.

[22] Y. Shimogonya, T. Ishikawa, Y. Imai, N. Matsuki, and T. Yamaguchi. Can temporal fluctuation in spatial wall shear stress gradient initiate a cerebral aneurysm? a proposed novel hemodynamic index, the gradient oscillatory number (gon). *Journal of biomechanics*, 42(4):550–554, 2009.

[23] R. Torii, M. Oshima, T. Kobayashi, K. Takagi, and T. E. Tezduyar. Fluid-structure interaction modeling of aneurysmal conditions with high and normal blood pressures. *Computational Mechanics*, 38:482–490, 2006.

[24] H. Ujiie, Y. Tamano, K. Sasaki, and T. Hori. Is the aspect ratio a reliable index for predicting the rupture of a saccular aneurysm? *Neurosurgery*, 48:495–502, 2001.

[25] K. Valen-Sendstad, K.-A. Mardal, and D. A. Steinman. High-resolution computational fluid dynamics detects high-frequency velocity fluctuations in bifurcation, but not sidewall, aneurysms of the middle cerebral artery. *Journal of biomechanics*, 2012.

[26] J. van Gijn, R. S. Kerr, G. J. Rinkel, et al. Subarachnoid haemorrhage. *Lancet*, 369(9558):306–318, 2007.

[27] J. Xiang, S. K. Natarajan, M. Tremmel, D. Ma, J. Mocco, L. N. Hopkins, A. H. Siddiqui, E. I. Levy, and H. Meng. Hemodynamic–morphologic discriminants for intracranial aneurysm rupture. *Stroke*, 42(1):144–152, 2011.

[28] Øyvind Evju. Sensitivity analysis of simulated blood flow in cerebral aneurysms. Master's thesis, University of Oslo, August 2011.